Effective radiative forcing and adjustments in CMIP6 models

Christopher J. Smith[1], Ryan J. Kramer[2,3], Gunnar Myhre[4], Kari Alterskjær[4], William Collins[5],
Adriana Sima[6], Olivier Boucher[6], Jean-Louis Dufresne[6], Pierre Nabat[7], Martine Michou[7],
Seiji Yukimoto[8], Jason Cole[9], David Paynter[10], Hideo Shiogama[11,12], Fiona M. O'Connor[13],
Eddy Robertson[13], Andy Wiltshire[13], Timothy Andrews[13], Cécile Hannay[14], Ron Miller[15],
Larissa Nazarenko[15], Alf Kirkevåg[16], Dirk Olivié[16], Stephanie Fiedler[17], Robert Pincus[18,19], and Piers
M. Forster[1]

[1]School of Earth & Environment, University of Leeds, LS2 9JT, UK
[2]Climate and Radiation Laboratory, NASA Goddard Space Flight Center, Greenbelt, MD 20771, USA
[3]Universities Space Research Association, 7178 Columbia Gateway Drive, Columbia, MD 21046, USA
[4]CICERO, Oslo, Norway
[5]Department of Meteorology, University of Reading, Reading, UK
[6]Laboratoire de Météorologie Dynamique, Institut Pierre-Simon Laplace, Sorbonne Université / CNRS, 4 Place Jussieu,
75252 Paris Cedex 05, France
[7]CNRM, Université de Toulouse, Météo-France, CNRS, Toulouse, France
[8]Meteorological Research Institute, Tsukuba, Japan
[9]Canadian Centre for Climate Modelling and Analysis, Environment Canada, Victoria, British Columbia, Canada
[10]Geophysical Fluid Dynamics Laboratory, Princeton University Forrestal Campus, 201 Forrestal Road, Princeton, NJ
08540-6649
[11]Center for Global Environmental Research, National Institute for Environmental Studies, 16-2 Onogawa, Tsukuba, Ibaraki
305-8506, Japan
[12]Atmosphere and Ocean Research Institute, University of Tokyo, 5-1-5 Kashiwanoha, Kashiwa, Chiba 277-8564, Japan
[13]Met Office Hadley Centre, FitzRoy Road, Exeter, EX1 3PB, UK
[14]NCAR/UCAR, Boulder, Colorado, USA
[15]NASA Goddard Institute for Space Studies, New York, NY 10025 USA
[16]Norwegian Meteorological Institute, Oslo, Norway
[17]Max-Planck-Institut für Meteorologie, Hamburg, Germany
[18]Cooperative Institute for Research in Environmental Sciences, University of Colorado Boulder, CO, USA
[19]NOAA/ESRL Physical Sciences Division, Boulder, CO, USA

Correspondence: C.J. Smith (c.j.smith1@leeds.ac.uk)

Abstract. The effective radiative forcing, which includes the instantaneous forcing plus adjustments from the atmosphere and surface, has emerged as the key metric of evaluating human and natural influence on the climate. We evaluate effective radiative forcing and adjustments in 13 contemporary climate models that are participating in CMIP6 and have contributed to the Radiative Forcing Model Intercomparison Project (RFMIP). Present-day (2014) global mean anthropogenic forcing relative to pre-industrial (1850) from climate models stands at 1.97 ($\pm$ 0.26) W m^{-2}, comprised of 1.80 ($\pm$ 0.11) W m^{-2} from CO_2, 1.07 ($\pm$ 0.21) W m^{-2} from other well-mixed greenhouse gases, -1.04 ($\pm$ 0.23) W m^{-2} from aerosols and -0.08 ($\pm$ 0.14) W m^{-2} from land use change. Quoted uncertainties are one standard deviation across model best estimates, and 90% confidence in the reported forcings, due to internal variability, is typically within 0.1 W m^{-2}. The majority of the remaining 0.17 W m^{-2} is likely to be from ozone. As determined in previous studies, cancellation of tropospheric and surface adjustments means that

10 the "traditional" stratospherically adjusted radiative forcing is approximately equal to ERF for greenhouse gas forcing, but not for aerosols, and consequentially, not for the anthropogenic total. The spread of aerosol forcing ranges from -0.63 to -1.37 W m^{-2}, exhibiting a less negative mean and narrower range compared to 10 CMIP5 models. The spread in $4\times CO_2$ forcing has also narrowed in CMIP6 compared to 13 CMIP5 models. Aerosol forcing is uncorrelated with equilibrium climate sensitivity. Therefore, there is no evidence to suggest that the increasing spread in climate sensitivity in CMIP6 models, particularly related to high-sensitivity models, is a consequence of a stronger negative present-day aerosol forcing.

1   Introduction

The effective radiative forcing (ERF) has gained acceptance as the most appropriate measure of defining the impact on the Earth's energy imbalance to a radiative perturbation (Myhre et al., 2013; Boucher et al., 2013; Forster et al., 2016). These perturbations can be anthropogenic or natural in origin, and include changes in greenhouse gas concentrations, aerosol burdens, land use characteristics, solar activity, and volcanic eruptions. A desirable aspect of ERF is that long-term equilibrium temperatures correspond better to ERF than to the long-used stratospherically-adjusted radiative forcing (RF) in the simple forcing-feedback relationship of the Earth's atmosphere:

$$\Delta N = F - \lambda \Delta T \tag{1}$$

where ΔN, F, λ and ΔT are the top-of-atmosphere (TOA) energy imbalance, (effective) radiative forcing, climate feedback parameter, and change in global-mean surface air temperature respectively. Richardson et al. (2019) showed that using ERF rather than RF reduces the need for forcing-specific efficacy values (the temperature response per unit forcing), first introduced by Hansen et al. (2005) as an observation that different values of λ better predicted ΔT for different forcing agents under RF. Conversely, evaluating ERF is less straightforward than RF, requiring climate model integrations, and numerous different methods of calculating ERF exist with their own benefits and drawbacks (Shine et al., 2003; Gregory et al., 2004; Hansen et al., 2005; Forster et al., 2016; Tang et al., 2019; Richardson et al., 2019).

The difference between ERF and RF is that ERF includes all tropospheric and land-surface adjustments whereas RF only includes the adjustment due to stratospheric temperature change (Sherwood et al., 2015; Myhre et al., 2013). Adjustments are often termed "rapid" (Myhre et al., 2013; Smith et al., 2018), however, there is no formal separation of adjustments and climate feedbacks based on timescale alone (Sherwood et al., 2015). It is conceptually more appropriate to divide adjustments as those changes in state that occur purely as a result of the action of a forcing agent from slow feedbacks that occur as a result of a change in global mean surface temperature. The instantaneous radiative forcing (IRF) is the initial perturbation to the Earth's radiation budget and unlike the RF and ERF does not include adjustments. By analysing atmosphere-only climate simulations using fixed climatological sea-surface temperatures (SSTs) and sea ice distributions, surface temperature driven

40 feedbacks are largely suppressed except for a small contribution from land surface warming or cooling (Vial et al., 2013; Tang et al., 2019), allowing for adjustments to be diagnosed from atmospheric state changes (Forster et al., 2016; Smith et al., 2018). This provides insight into the mechanisms contributing to the effective radiative forcing. For example, the ERF of black carbon is half of the impact estimated from its IRF as a consequence of its strong atmospheric absorption and adjustments arising from how it perturbs tropospheric heating rates, affecting the distribution of tropospheric temperatures, water vapour and clouds

45 (Stjern et al., 2017; Smith et al., 2018; Johnson et al., 2019; Allen et al., 2019).

The experimental protocol for determining (effective) radiative forcing in models has been extended since Phase 5 of the Coupled Model Intercomparison Project (CMIP5). CMIP5 included experiments for present-day (year 2000) all-aerosol and sulfate-only forcing (Zelinka et al., 2014, CMIP5 experiment labels sstClimAerosol and sstClimSulfate), and $4\times CO_2$ forcing (sstClim4xCO2; Andrews et al., 2012; Kamae and Watanabe, 2012) with respect to a pre-industrial baseline with climatological

50 SSTs and sea ice distributions (sstClim). A handful of IRF outputs from quadrupled CO_2 experiments (Chung and Soden, 2015) were also obtained. For CMIP6, the Radiative Forcing Model Intercomparison Project (RFMIP; Pincus et al., 2016) provides a number of present-day time-slice and historical-to-future transient experiments designed to evaluate the ERF in climate models for different forcing agents, providing insight into why climate models respond the way they do to particular forcings. This is important when diagnosing climate feedbacks (Forster et al., 2013), given the role of forcing in the Earth's energy budget

55 (eq. (1)), and knowledge of forcing is required for attribution of historical temperature change (Haustein et al., 2017) and in future scenario projections (Gidden et al., 2019). Effective radiative forcings derived from models can be used to validate assumptions derived from other lines of evidence, particularly for aerosol forcing, as is done by the Intergovernmental Panel on Climate Change (IPCC) in their periodic Assessment Reports.

2 Models and experimental protocol

60 We use results from 13 state-of-the-art atmospheric general circulation models (GCMs) and Earth system models (ESMs) contributing to Tier 1 of RFMIP (table 1) as part of CMIP6 (Eyring et al., 2016). Models with diagnostics available on the Earth System Grid Foundation (ESGF) up until 19 December 2019 have been analysed. Each model is run in atmosphere-only mode using pre-industrial climatologies of sea-surface temperatures (SSTs) and sea-ice distributions from at least 30 years of the same model's corresponding coupled pre-industrial control run (piControl, Eyring et al. (2016)). RFMIP's Tier

65 1 calls for 30-year timeslice experiments forced with $4\times$ pre-industrial CO_2 concentrations (RFMIP name piClim-4xCO2), all present-day anthropogenic forcers (piClim-anthro), present-day well-mixed greenhouse gases (piClim-ghg), present-day aerosols (piClim-aer) and present-day land use (piClim-lu) in this fixed-SST configuration. All forcing components that are not perturbed in a particular experiment remain at pre-industrial (year 1850) values, and "present-day" is defined as year 2014 conditions. A 30-year experiment with pre-industrial conditions, piClim-control, is also performed as a reference case, and all

70 results presented in this paper are with reference to piClim-control, accounting for the fact that models may not be in precise radiative equilibrium. Results from the $4\times CO_2$ experiment are also rescaled to the ratio of 2014 to 1850 CO_2 concentrations of approximately $1.4\times$ pre-industrial by a factor of 0.2266, being the ratio of RF from $1.4\times CO_2$ to $4\times CO_2$ from the Etminan

Table 1. Contributing climate models to RFMIP-ERF Tier 1. The adjustment time is based on approximately how long stratospheric temperatures take to equilibrate in the $4\times CO_2$ experiment (fig. 2). ISCCP simulator diagnostics are indicated where existent.

Model	Atmospheric resolution (lon $\times$ lat)	Adjustment timescale (yr)	Model years	ISCCP simulator	Reference
CanESM5	$2.81° \times 2.81°$, 49 levels to 1 hPa	1	50	all	Swart et al. (2019)
CESM2	$1.25° \times 0.9°$, 32 levels to 2.25 hPa	1	30	ghg, aer, lu, anthro	Danabasoglu et al. (submitted)
CNRM-CM6-1	$1.4° \times 1.4°$, 91 levels to 0.01 hPa	5	30	CO_2, ghg, aer, lu	Voldoire et al. (2019)
CNRM-ESM2-1	$1.4° \times 1.4°$, 91 levels to 0.01 hPa	15	30	all	Séférian et al. (2019)
GFDL-CM4	$1.25° \times 1°$, 33 levels to 1 hPa	1	30	all	Held et al. (2019)
GISS-E2-1-G[1]	$2.5° \times 2°$, 40 levels to 0.1 hPa	5	31		Schmidt et al. (2014)
HadGEM3-GC31-LL	$1.875° \times 1.25°$, 85 levels to 85 km	1	30	all	Williams et al. (2018)
IPSL-CM6A-LR	$2.5° \times 1.27°$, 79 levels to 80 km	10	30	all	Boucher et al. (submitted)
MIROC6	$1.4° \times 1.4°$, 81 levels up to 0.004 hPa	1	30	aer	Tatebe et al. (2019)
MPI-ESM1-2-LR	$1.875° \times 1.875°$, 47 levels up to 0.01 hPa	1	31		Mauritsen et al. (2019)
MRI-ESM2-0	$1.125° \times 1.125°$, 80 levels to 0.01 hPa	1	30	all	Yukimoto et al. (2019)
NorESM2-LM	$2.5° \times 1.875°$, 32 levels to 3 hPa	1	30		Seland et al., in prep. Olivié et al., in prep. Kirkevåg et al. (2018)
UKESM1-0-LL	$1.875° \times 1.25°$, 85 levels to 85 km	3	45[2]	CO_2, aer, lu, anthro	Sellar et al. (2019)

1. GISS-E2-1-G produced two physics versions for piClim-control and piClim-aer; physics_version=1 includes aerosol and ozone specified by pre-computed transient fields and physics_version=3 includes aerosol-cloud interactions. Only physics_version=1 is analysed in this paper.

2. 40 years for piClim-4xCO2

et al. (2016) formula. This is performed to isolate an estimate of the CO_2-only contribution to the present-day forcing, and is based on year-1850 and year-2014 CO_2 concentrations of 284.32 and 397.55 ppm respectively (Meinshausen et al., 2017) along with the 1850 concentrations of 808.25 ppb for CH_4 and 273.02 ppb for N_2O. Except where explicitly stated, we present results from this experiment as $1.4\times CO_2$.

The experiments and results presented in this study follow on from the assessment of ERF and adjustments in 11 models contributing to the Precipitation Driver and Response Model Intercomparison Project (PDRMIP, see Myhre et al., 2017) in Smith et al. (2018). In Smith et al. (2018) idealised experiments of $2\times CO_2$ concentrations, $3\times CH_4$ concentrations, $10\times$ black carbon (BC) emissions or burdens, $5\times SO_4$ emissions or burdens and a 2% solar constant increase were analysed from CMIP5-era and interim models. Only the $4\times CO_2$ experiment has a similar experiment for comparison in Smith et al. (2018), whereas the RFMIP protocol focuses more on combinations of anthropogenic forcers. In addition, extended model diagnostics allow us to determine cloud responses and aerosol forcing in more detail in this study.

3 Effective radiative forcing

85 Using climatological SSTs allows for ERF to be diagnosed as the difference of top-of-atmosphere net radiative flux between a given forcing experiment and a pre-industrial control simulation (Hansen et al., 2005). Using 30 year timeslices generally results in standard absolute errors of less than 0.1 W m^{-2} (Forster et al., 2016). Although inter-annual variability affects the diagnosed ERF using this climatological SST method, the standard error in the estimates obtained is much smaller than using a fully-coupled ocean-atmosphere model with a Gregory regression (Gregory et al., 2004), and as such fewer model years are 90 needed to diagnose ERF. Two advantages of this is that it reduces the computational burden for modelling centres, and can also be used to diagnose forcings of the order of 0.1 W m^{-2} (Forster et al., 2016). For this reason, the climatological-SST method is implemented to derive forcing in RFMIP, and ERF in this paper (without qualifier) is taken to mean this.

The climatological-SST method of deriving ERF includes the TOA flux changes resulting from land-surface warming or cooling as part of the ERF. Conceptually, any land-surface temperature change as a response to forcing should be excluded 95 in the same way that SST changes are (Shine et al., 2003; Hansen et al., 2005; Vial et al., 2013), but in general, prescribing land surface temperatures is difficult in GCMs and this has not been performed in RFMIP. In essence, the goal is to completely isolate the forcing from any surface temperature change (ΔT) or feedbacks (λ) in eq. (1). We test several methods to correct for adjustments to attempt to isolate forcing at $\Delta T = 0$ (also performed in Richardson et al. (2019); Tang et al. (2019)):

– *Effective radiative forcing (ERF)* is reserved to mean the TOA flux difference between a perturbed and control simulation, 100 with climatological SSTs and sea ice distributions and no correction for land surface temperature change, as in Hansen et al. (2005); Myhre et al. (2013); Forster et al. (2016); Smith et al. (2018).

– *Effective radiative forcing using a Gregory regression (ERF_reg)* is calculated from each model's CMIP abrupt4xCO2 experiment by regressing the annual temperature anomaly compared to the same model's pre-industrial control (piControl) against the annual TOA energy imbalance anomaly ΔN (eq. (1)) and finding the intercept at $\Delta T = 0$, as in Gregory 105 et al. (2004). It is only possible to determine for $4 \times CO_2$ as coupled abrupt forcing experiments are not performed for other forcing agents as part of CMIP6.

– *Stratospherically adjusted radiative forcing (RF):* All tropospheric and surface adjustments, calculated using radiative kernels (section 4) are subtracted from the ERF, leaving just the stratospheric temperature adjustment to the IRF. The RF is included for historical comparison, although it is usually calculated using an offline method such as fixed dynamical 110 heating (Forster and Shine, 1997). It should be noted that the stratospheric adjustment is included in all definitions of ERF.

– *Land-surface corrected effective radiative forcing (ERF_ts):* Land surface temperature change adjustment is subtracted from the climatological-SST ERF using the surface temperature radiative kernel.

– *Tropospherically corrected effective radiative forcing (ERF_trop)*: In addition to land-surface warming a proportion of 115 tropospheric temperature and water vapour change is subtracted from the ERF using radiative kernels, by assuming a

Table 2. Effective radiative forcing from each Tier 1 time-slice RFMIP experiment for each model (W m^{-2}). Also shown is the $4\times CO_2$ ERF scaled to 2014 concentrations (as $1.4\times CO_2$). WMGHGs = well-mixed greenhouse gases.

Model	$4\times CO_2$	$1.4\times CO_2$	WMGHGs	aerosols	land-use	anthropogenic
CanESM5	7.61	1.72	2.87	−0.85	−0.08	2.37
CESM2	8.91	2.02	3.03	−1.37	−0.04	2.05
CNRM-CM6-1	8.00	1.81	2.74	−1.15		1.61
CNRM-ESM2-1	7.93	1.80	2.51	−0.74	−0.07	1.66
GFDL-CM4	8.24	1.87	3.13	−0.73	−0.33	2.34
GISS-E2-1-G	6.90	1.56	2.89	−1.32	−0.00	1.93
HadGEM3-GC31-LL	8.09	1.83	3.11	−1.10	−0.11	1.81
IPSL-CM6A-LR	8.00	1.81	2.82	−0.63	−0.05	2.32
MIROC6	7.32	1.66	2.69	−1.04	−0.03	1.80
MPI-ESM1-2-LR	8.35	1.89	2.69		−0.10	
MRI-ESM2-0	7.65	1.73	3.03	−1.21	−0.17	1.95
NorESM2-LM	8.15	1.85	2.80	−1.21	0.26	2.06
UKESM1-0-LL	7.94	1.80	2.94	−1.13	−0.30	1.71
Mean	7.93	1.80	2.87	−1.04	−0.08	1.97
Standard dev.	0.47	0.11	0.18	0.23	0.14	0.26

fixed lapse rate in the troposphere based on the land surface temperature change. The remaining tropospheric temperature change when the constant lapse rate is subtracted is treated as the tropospheric temperature adjustment. The water vapour correction from the land surface warming is taken as the fraction of the adjustment from the constant lapse rate to the total tropospheric temperature adjustment. The land surface temperature change and land surface albedo change are added, whereas no cloud adjustment is included justified by cloud adjustments to a large extent depending on heating/cooling in the troposphere (Smith et al., 2018). This was known as ERF_kernel in Tang et al. (2019).

– *Feedback corrected effective radiative forcing (ERF_λ):* An amount corresponding to the global-average near-surface air temperature (GSAT) warming multiplied by the model's climate feedback parameter from its corresponding CMIP abrupt4xCO2 run is subtracted from the fixed-SST ERF. The same value of λ from abrupt4xCO2 is applied to the GSAT change in all experiments. This method was first investigated by Hansen et al. (2005) and is known as ERF_fSST_ΔTland in Tang et al. (2019).

Table 2 shows the ERF diagnosed from each forcing and each model using the climatological-SST method, and fig. 1 shows the ERF, diagnosed IRF, and adjustments from each RFMIP Tier 1 experiment. Instantaneous forcing (IRF) is calculated as the difference of the ERF and the sum of adjustments, with exception being land-use forcing where IRF is calculated directly
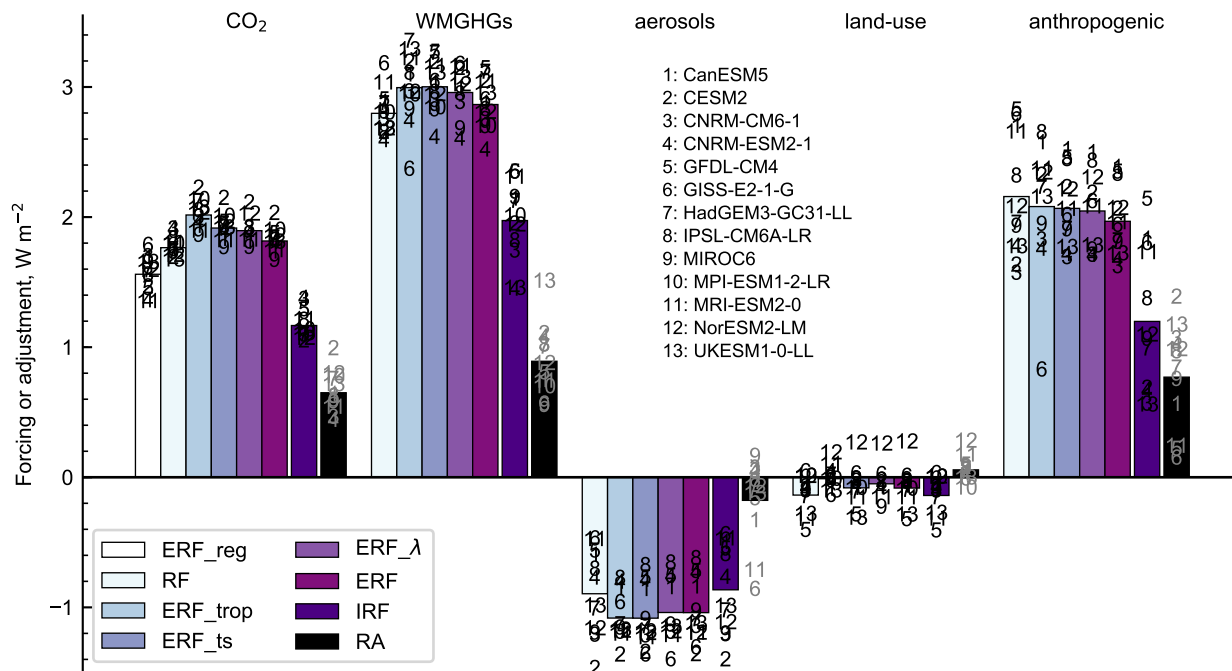
Figure 1. Comparison of radiative forcing (RF, which by definition includes stratospheric temperature adjustment), effective radiative forcing with tropospheric correction (ERF_trop), effective radiative forcing with land-surface kernel correction (ERF_ts), feedback-corrected ERF (ERF_λ), and fixed-SST ERF. For CO_2 forcing, ERF from a Gregory regression (ERF_reg) from each model's corresponding abrupt4xCO2 CMIP simulation is also given. The ERF is compared with the IRF and adjustments (RA) for each of the present-day RFMIP-ERF time slice experiments (1.4×CO_2 is shown instead of 4×CO_2 for better comparison with other forcing agents). Individual models are numbered.

130 from the surface albedo kernel. In keeping with the definitions of ERF and adjustments, IRF is defined at the TOA in this study. Adjustment calculations are explained in detail in section 4.

For ease of comparison we show 1.4×CO_2 instead of 4×CO_2, with the scaling to present-day concentrations assumed to apply to ERF, IRF and all adjustments proportionally. Figure 1 also shows the ERF_reg (for 4×CO_2), ERF_ts, ERF_λ and RF. In general, the methods that correct for land surface temperature change (ERF_ts, ERF_trop and ERF_λ) result in forcings that

135 are slightly stronger than non-corrected ERF, although differences between these methods are comparable to the magnitude of internal year-to-year variability and small compared to the contribution of adjustments. The exception is for ERF_trop for 1.4×CO_2, where there is substantial land-surface warming that contributes to tropospheric warming under the fixed lapse-rate assumption. For CO_2 in fig. 1 we exclude GISS-E2-1-G (model 6) due to an anomalous tropospheric cooling that biases ERF_trop. For CO_2, ERF_reg results in a lower estimate of ERF than any of the fixed-SST methods (Forster et al., 2016),

140 which is possibly due to the non-linear nature of how climate feedbacks evolve over time in coupled model runs (Armour, 2017) and any change in pattern of SSTs that are not included in the climatological-SST ERF.

4 Forcing adjustments

4.1 Non-cloud adjustments

Adjustments to the radiative forcing describe flux changes resulting from changing atmospheric or surface state, in response to a forcing, but unrelated to the change in globally-averaged surface temperature (thus decoupling them from climate feedbacks, Myhre et al. (2013); Sherwood et al. (2015)). Adjustments to non-cloud changes in this study are calculated using radiative kernels (Chung and Soden, 2015; Vial et al., 2013; Smith et al., 2018). The difference in an atmospheric state variable x (air temperature, surface temperature, specific humidity or surface albedo) between a forcing perturbation (pert) and piClim-control (base) is multiplied by the kernel K_x to derive the adjustment A_x:

$$A_x = K_x(x_{\text{pert}} - x_{\text{base}}) \qquad (2)$$

The radiative kernel describes the change in TOA fluxes for a unit change in state for $x \in \{T, T_s, q, \alpha\}$ where T is atmospheric air temperature, T_s is surface temperature, q is water vapour and α is surface albedo. K_T and K_q are four-dimensional (month, pressure level, latitude, longitude) and K_{T_s} and K_α are three dimensional (month, latitude, longitude). Kernels are produced for both longwave and shortwave radiation changes. Typical unit changes are 1 K for temperature, the change in specific humidity that maintains constant relative humidity for a temperature increase of 1 K for water vapour, and 1% additive for surface albedo. For the division of temperature into stratospheric and tropospheric components, the WMO definition of the lapse-rate tropopause is used from each model's piClim-control run, using geopotential height as an approximation of geometric height on model pressure levels.

The water vapour kernel describes the change in TOA flux for a perturbation that maintains relative humidity for an increase in specific humidity corresponding to a temperature increase of 1 K in the kernel climatology. The assumption therefore is that relative humidity is approximately constant in the perturbation and control runs, which is found to be true in coupled experiments where changes in specific humidity are larger than in this study due to surface-temperature driven feedbacks (Held and Soden, 2000). Note that the difference in states is taken for the logarithm of water vapour concentration in eq. (2). More details on the application of the kernel method can be found in Smith et al. (2018, Supplementary Material).

In this paper we use radiative kernels derived from the atmospheric component of the HadGEM3-GC31-LL model (HadGEM3-GA7.1), interpolated to the 19 standard CMIP6 pressure levels (Smith et al., submitted). With the exception of stratospheric temperature adjustments to greenhouse-gas forcing, structural differences introduced by using different kernels are well within 0.1 W m^{-2} (Soden et al., 2008; Smith et al., 2018), and the HadGEM3-GA7.1 kernel is representative of the population of radiative kernels commonly used in the literature for tropospheric and surface adjustments (fig. S1); we use this particular kernel for its improved stratospheric resolution as outlined in Smith et al. (submitted).

Stratospheric adjustments to greenhouse-gas driven experiments are expected to equilibriate within a few model months (Sherwood et al., 2015). We find that the time to reach equilibrium varies between models for a 4×CO$_2$ forcing. Figure 2 shows the time taken for the stratospheric temperature adjustment, and hence stratospheric temperatures, to adjust to a 4×CO$_2$ forcing. In CNRM-ESM2-1, concentrations of CO$_2$ are relaxed towards the 4× pre-industrial level below 560 hPa, and al-
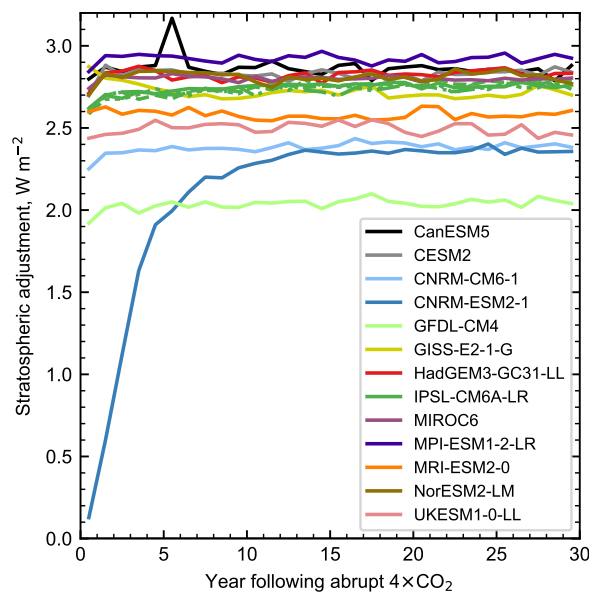
Figure 2. Transient response of the stratospheric temperature adjustment to a $4\times CO_2$ forcing. The small spike in year 6 in CanESM5 is due to an unseasonably low tropical tropopause in July of year 6, resulting in much of the temperature adjustment at the 100 hPa level to be counted in the stratosphere.

175 lowed to propagate throughout the atmosphere, therefore taking around 15 years to reach an approximate uniform atmospheric concentration. This is in contrast to the physical climate model from the same group (CNRM-CM6-1). However, even in some physical models, we find that the time to reach equilibrium varies between models and may be up to 10 years (e.g. in IPSL-CM6A-LR; fig. 2). For this reason, we discard the first few years of model output where the stratosphere is still adjusting to a forcing for the $4\times CO_2$, well-mixed greenhouse gas (WMGHG) and anthropogenic forcing experiments (table 1). We find

180 this issue is not present in the aerosol or land-use experiments. It is important to emphasise that our stratospheric adjustment is calculated in a different way to the usual RF method which uses an offline radiative transfer method. It may therefore be the case that differences are due to a change in tropopause height in greenhouse-gas -driven experiments (Santer et al., 2003).

4.2 Cloud adjustments

The radiative effect of clouds depends on their coverage (both within layer and total), ice water content, liquid water content,
185 droplet effective radius and ice particle habit. Cloud properties vary extensively from model to model, and unlike pressure level diagnostics of temperature and humidity, cloud diagnostics are not output on 19 standard pressure levels in CMIP. A number of different approaches have therefore been used to estimate cloud adjustments, depending on availability of diagnostics and model specific setup. Where cloud adjustments can be calculated with more than one method, we take the mean of each available method.

4.2.1 ISCCP simulator kernel

The ISCCP simulator cloud kernel (Zelinka et al., 2012) allows diagnosis of flux changes due to clouds from ISCCP simulator diagnostics. The ISCCP simulator algorithm (Klein and Jakob, 1999; Webb et al., 2001) maps model-native clouds into cloud types that would be reported by ISCCP satellites (Rossow et al., 1996), which is a 7×7 histogram of cloud optical thickness (τ) and cloud top pressure (CTP). Ten models included ISCCP simulator diagnostics within their RFMIP output (table 1).

The ISCCP simulator kernel reports all flux changes resulting from clouds. For CO_2, WMGHG and land-use forcings, it is assumed that cloud droplet effective radius does not change as aerosols do not change (except for NorESM2-LM, but this model did not include ISCCP simulator diagnostics), and therefore in these experiments the SW flux changes from the ISCCP simulator kernel are treated as the cloud adjustment. For aerosol and total anthropogenic forcing this is usually not the case as most models include aerosol-radiation interactions (significant in the SW), with ice particle behaviour also changing in the MRI-ESM-2.0, MIROC6 and CESM2 models which affects LW fluxes. NorESM2-LM also includes the effects of mineral dust and BC on heterogeneous ice nucleation (Kirkevåg et al., 2018). Following Boucher et al. (2013) we treat the cloud-albedo response to aerosols as part of the IRF, and the ISCCP simulator kernel is unable to separate this effect from any rapid adjustment. We assume that any LW effect from aerosol-cloud interactions is small except in those models that include aerosol effects on ice clouds.

4.2.2 Approximate partial radiative perturbation with liquid water path adjustment

With no changes in aerosol forcing, the changes in cloud absorption, cloud scattering and cloud amount calculated from the approximate partial radiative perturbation method (APRP; section 5.3.3) can be taken to be the SW cloud adjustment. We use this estimate for CO_2, WMGHG and land-use forcing.

For aerosol forcing, the effect of cloud amount changes calculated by APRP (A_{CLT}) is an adjustment, but the cloud scattering is a combination of radiative forcing due to aerosol-cloud interactions (RFaci), treated as part of the IRF, and adjustments due to cloud liquid water path (LWP) changes (A_{LWP}; Bellouin et al., in press). For the LWP adjustment we use a relationship obtained in Gryspeerdt et al. (2019) in which LWP adjustment (W m^{-2}) scales linearly with vertically integrated in-cloud liquid water path (kg m^{-2}):

$$A_{\mathrm{LWP}} = -\frac{1000}{37.6}\left(\frac{\mathrm{clwvi_{pert}} - \mathrm{clivi_{pert}}}{\mathrm{clt_{pert}}/100} - \frac{\mathrm{clwvi_{base}} - \mathrm{clivi_{base}}}{\mathrm{clt_{base}}/100}\right). \tag{3}$$

In eq. (3), clwvi, clivi and clt are the CMIP6 variable labels for total cloud water path, ice water path and total cloud fraction in percent. We then isolate the RFaci as

$$\mathrm{RFaci} = \mathrm{ERFaci} - A_{\mathrm{LWP}} - A_{\mathrm{CLT}}. \tag{4}$$

with ERFaci, the effective radiative forcing due to aerosol-cloud interactions, calculated from APRP (section 5.3.3).

For anthropogenic total forcing, the RFaci calculated in eq. (4) from the aerosol forcing experiment is subtracted from the total derived cloud change under APRP, which includes contributions from greenhouse gases and land use as well as RFaci. For

models not including ice cloud nucleation, the LW cloud adjustment for aerosols is estimated from the cloud radiative effect. For other experiments this results in a biased estimate of cloud adjustment due to masking of LW adjustments.

4.2.3 Offline monthly mean partial radiative perturbation

Not all models provide ISCCP simulator diagnostics so for LW cloud adjustments we also produce an offline simulation using

225 the SOCRATES radiative transfer code (Edwards and Slingo, 1996). This is produced by substituting fields of cloud fraction, cloud water content and cloud ice content from each model and experiment into a climatology for the year 2014 provided by ERA5 (Copernicus Climate Change Service, 2017). Taking the cloud fields in each experiment minus those from the control gives $A_{\mathrm{LWP}} + A_{\mathrm{CLT}}$ in each model. This offline substitution method is performed for years 16–25 of each model's output. As only monthly mean diagnostics are available from models in general, we only attempt this in the LW which is assumed

230 to be less biased than the SW (Mülmenstädt et al., 2019; Bellouin et al., submitted). The monthly mean cloud fraction, ice water content and liquid water content variables in all experiments are scaled by a model-dependent factor that ranges between 0.68 and 1.5 to ensure that TOA LW outgoing flux is approximately 240 W m^{-2} in the control experiment, in line with TOA observations (Loeb et al., 2018).

4.2.4 Kernel masking

235 In the land-use experiment, IRF is directly estimated from the surface albedo kernel such that IRF = A_α. As there are no other unknowns in the kernel decomposition, cloud adjustments can be calculated using the kernel masking method (Soden et al., 2008), where

$$A_c = (\mathrm{ERF} - \mathrm{ERF}^{\mathrm{clr}}) - (A_\alpha - A_\alpha^{\mathrm{clr}}) - \sum_{i \in \{\mathrm{T}, \mathrm{T_s}, \mathrm{q}\}} (A_i - A_i^{\mathrm{clr}}) \tag{5}$$

where the clr superscript in eq. (5) refers to fluxes calculated with clear-sky radiative kernels.

5 Multi-model results

240

Figure 3 shows the contribution to the total adjustment in each experiment from land surface temperature, tropospheric temperature, stratospheric temperature, water vapour, surface albedo and clouds. No corrections for tropospheric or land surface warming as discussed in section 3 have been performed for these results.

Figure 4 shows the effect on TOA radiative flux arising from cloud responses from the ISCCP simulator for each experiment

245 from models that provided these diagnostics (table 1). In this figure, histogram boxes not marked with a cross are where 75% or more of the models agree on the sign of the cloud fraction or radiative flux change, following Zelinka et al. (2012).
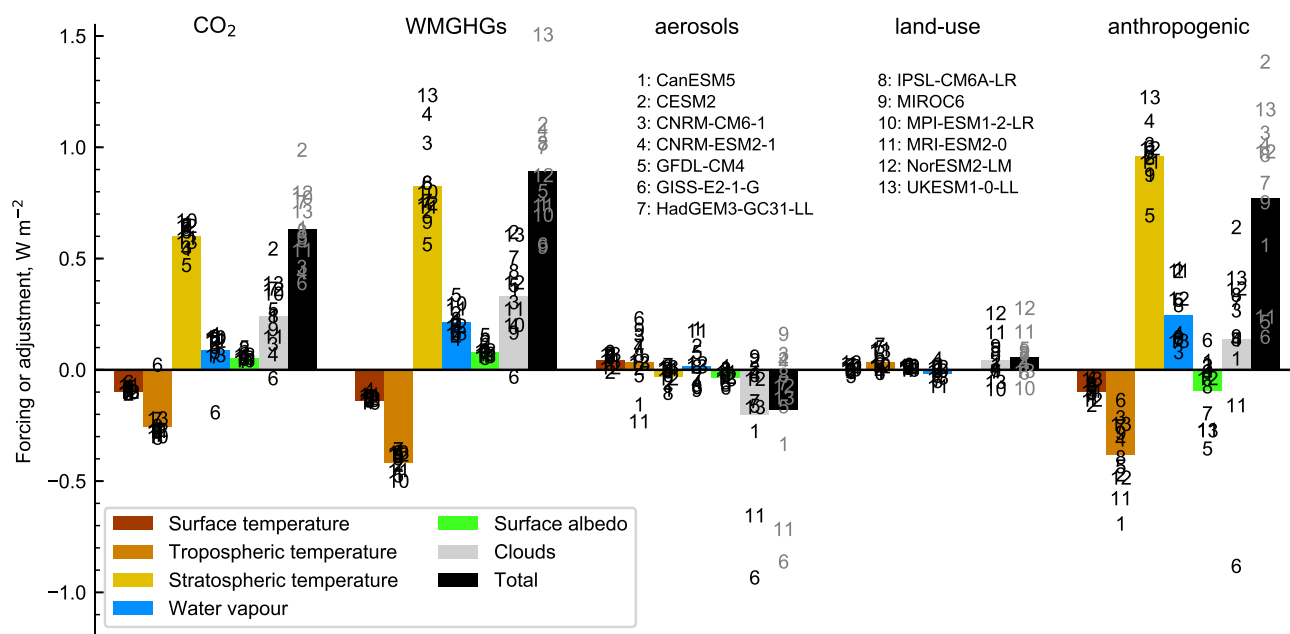
Figure 3. Adjustments broken down by mechanism in each of the present-day RFMIP-ERF time slice experiments. Black/grey circles indicate individual models, coloured bars indicate the multi-model mean.

5.1 Carbon dioxide

The multi-model mean ERF from a quadrupling of CO_2 is 7.93 W m^{-2} ($\pm$ 0.47 W m^{-2}; all uncertainties given as one standard deviation). This equates to an ERF for 2×CO_2 of 3.79 ($\pm$ 0.23) W m^{-2} scaled down using the Etminan et al. (2016) formula,

250 comparable to the best estimate of 3.71 W m^{-2} from the IPCC's Fifth Assessment Report (AR5; Myhre et al. (2013)). The Etminan et al. (2016) formula produces a value of 3.80 W m^{-2} for a doubling of CO_2 which is very close to our multi-model mean ERF. On this basis, our derived multi-model mean for 1.4×CO_2 is 1.80 ($\pm$ 0.11) W m^{-2}, which is the same result produced from the Etminan et al. (2016) formula. In individual models which have performed 1.4×CO_2 experiments, our scaled-down 4×CO_2 calculation produces very similar results (table S1). The Etminan et al. (2016) relationship produces a

255 CO_2 RF that increases faster than logarithmically, for which there is a growing body evidence (Hansen et al., 2005; Gregory et al., 2015; Colman and McAvaney, 2009; Jonko et al., 2013; Caballero and Huber, 2013; Boucher et al., submitted). As shown in fig. 1 and discussed in section 5.1, ERF is approximately equal to RF for CO_2, and we apply the Etminan formula to ERF.

The 4×CO_2 ERF from 13 CMIP6 models is larger, but not significantly so (p-value 0.19 using a Welch's t-test), than the 4×CO_2 ERF from 13 CMIP5 models of 7.53 ($\pm$0.89) W m^{-2} (Kamae and Watanabe, 2012). In addition, CMIP6 models are

260 notable for their smaller spread in CO_2 ERF than CMIP5 models. Zelinka et al. (accepted) show that ERF_reg for 4×CO_2 also increases in CMIP6 compared to CMIP5, and attribute 20% of the increase in multi-model mean equilibrium climate sensitivity (ECS) in CMIP6 to this. We note that a long standing problem in GCMs has been on the diversity in the forcing of CO_2 (Soden
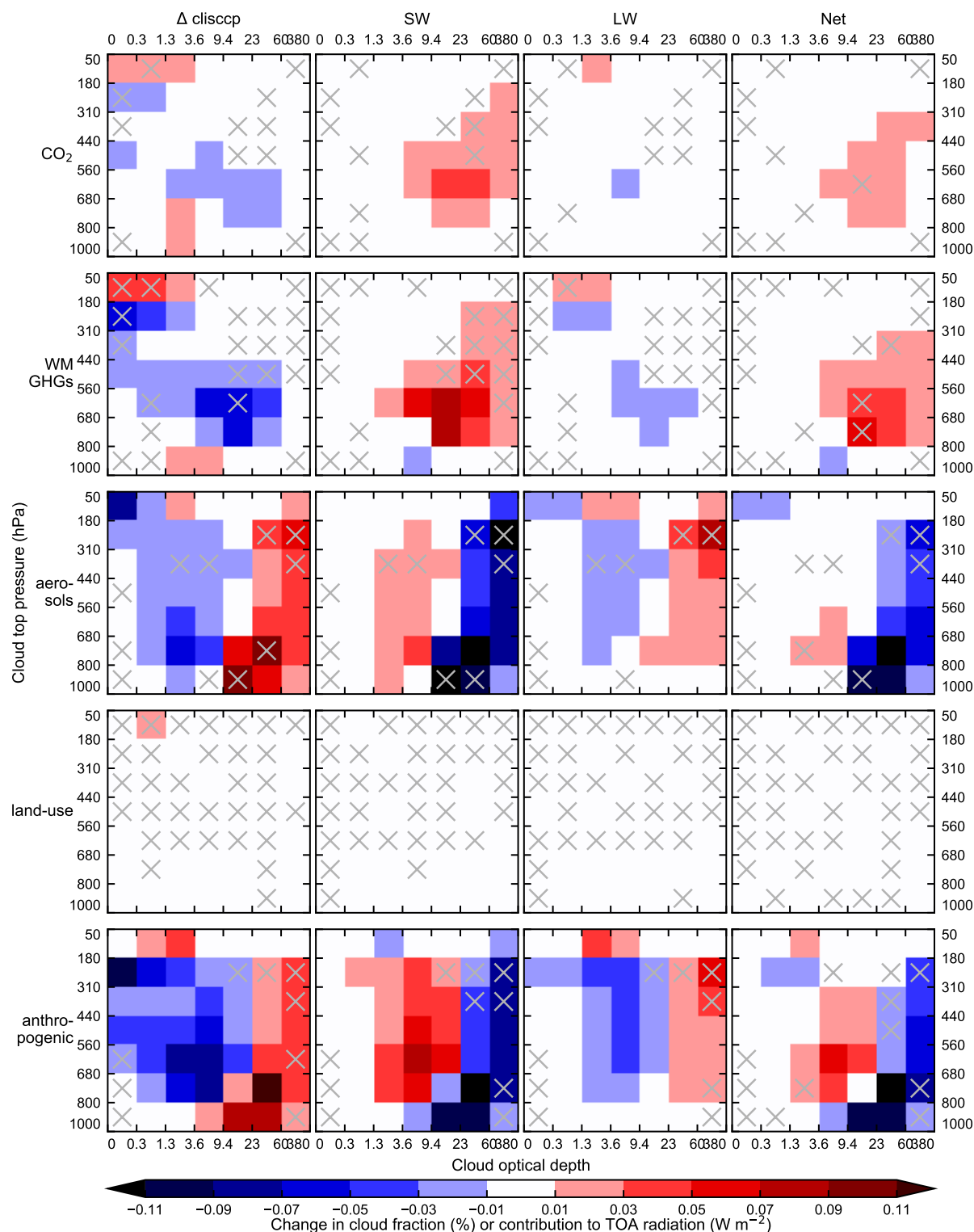
Figure 4. Global mean change in ISCCP-simulated cloud fraction in CTP-τ space (first column) and consequential changes in SW (second column), LW (third column) and net (fourth column) radiation when convoluted with the ISCCP cloud kernel. Grey crosses show where less than 75% of models agree on sign. Figure shows the multi-model mean cloud fraction and radiative effect. For $1.4\times CO_2$ the change in cloud fraction, as well as the radiative fluxes, are scaled down from the $4\times CO_2$ experiment using Etminan et al. (2016).

et al., 2018), which may result both from model broadband radiation parameterisation error in the IRF component (Pincus et al., 2015) and differences in base state climatology between models. The reduction in spread of CO_2 forcing in CMIP6 may be indicative that model radiation parameterisations are improving. In particular, in HadGEM3-GC31-LL, the IRF for $4\times CO_2$ is improved relative to previous versions of the model when comparing the GCM radiative transfer parameterisation to a narrowband radiative transfer model (Andrews et al., 2019).

Stratospheric temperature adjustment dominates for CO_2-driven simulations, which is well-known (Smith et al., 2018; Myhre et al., 2013). Tropospheric adjustments approximately sum to zero, such that the overall adjustment approximately equals the stratospheric adjustment, and RF is a good approximation to ERF (Smith et al., 2018). Nevertheless, individual tropsopheric adjustments are non-zero and significant. A warming land surface and troposphere leads to a negative adjustment (more outgoing LW radiation to space) that is partially offset by increased tropospheric water vapour (analogous to the water vapour feedback). Cloud adjustments are overall positive, dominated by a reduction in mid-troposphere clouds driven by tropospheric warming, leading to a positive SW radiative effect (fig. 4). The LW effect is small in comparison, so that the SW effect dominates the net cloud adjustment.

The GISS-E2-1-G model shows anomalous tropospheric behaviour compared to the other models, exhibiting a positive tropospheric temperature adjustment, negative water vapour adjustment and negative cloud adjustment. This effect is traced to a slight cooling in the mid-troposphere in this model whereas other models show a distinct warming. This phenomenon causes the ERF definition that relies on tropospheric corrections (ERF_trop) to differ significantly from other methods. Excluding this anomalous model, the largest spread in total adjustments are due to clouds.

The spatial pattern of adjustments is shown in fig. 5. In figs. 5 to 7, 11 and 12, cloud changes are only shown from the ISCCP simulator kernels in subfigures (g–i) and are not the means of all participating models, whereas ERF and non-cloud adjustments in (a–f) are multi-model means. Stratospheric cooling is spatially uniform and results in a robustly positive adjustment of $+0.60$ W m^{-2}, i.e. one third of the total ERF. Tropospheric temperature adjustments are globally negative and robust over much of the Northern Hemisphere. Cloud changes show several robust spatial patterns, including positive changes over Eurasia and North America land.

5.2 Well-mixed greenhouse gases

The ERF from all well-mixed greenhouse gases is evaluated to be 2.87 (± 0.18 W m^{-2}) for 1850–2014, implying a contribution of 1.07 (± 0.21) W m^{-2} from non-CO_2 WMGHGs (uncertainties in quadrature and this definition excludes changes in ozone). Tier 1 of RFMIP does not contain additional granularity to break down non-CO_2 forcing by species, however dedicated experiments to derive ERF from methane, nitrous oxide and halocarbons separately are part of the protocol for the Aerosol and Chemistry Model Intercomparison Project (AerChemMIP; Thornhill et al., submitted; Collins et al., 2017).

There is also a substantial adjustment arising from WMGHG forcing, and again this is mostly driven by stratospheric cooling implied by the observation that ERF and RF are approximately equal. This confirms PDRMIP model behaviour for CO_2 and CH_4 forcing (Smith et al., 2018), which found that tropospheric and land adjustments, while individually significant, approximately sum to zero leaving just the stratospheric temperature adjustment. Unlike in Smith et al. (2018), who found

Table 3. ERF, IRF and adjustments (W m^{-2}) by component from 1.4×CO$_2$, scaled down from the 4×CO$_2$ RFMIP experiment. ts=surface temperature, ta_tr=tropospheric temperature, ta_st=stratospheric temperature, hus=water vapour, albedo=surface albedo, cl=clouds.

Model	ERF	IRF	Adj.	ts	ta_tr	ta_st	hus	albedo	cl
CanESM5	1.72	1.09	0.63	−0.10	−0.30	0.65	0.10	0.05	0.23
CESM2	2.02	1.04	0.98	−0.12	−0.29	0.64	0.11	0.09	0.54
CNRM-CM6-1	1.81	1.36	0.45	−0.10	−0.29	0.54	0.14	0.05	0.11
CNRM-ESM2-1	1.80	1.37	0.43	−0.08	−0.28	0.53	0.15	0.05	0.06
GFDL-CM4	1.87	1.28	0.59	−0.09	−0.28	0.46	0.13	0.09	0.26
GISS-E2-1-G	1.56	1.18	0.38	−0.06	0.01	0.61	−0.20	0.06	−0.05
HadGEM3-GC31-LL	1.83	1.09	0.75	−0.11	−0.23	0.64	0.05	0.03	0.36
IPSL-CM6A-LR	1.81	1.20	0.61	−0.11	−0.31	0.62	0.14	0.04	0.23
MIROC6	1.66	1.09	0.57	−0.10	−0.26	0.63	0.07	0.05	0.17
MPI-ESM1-2-LR	1.89	1.12	0.77	−0.11	−0.31	0.66	0.14	0.05	0.33
MRI-ESM2-0	1.73	1.20	0.53	−0.08	−0.28	0.58	0.13	0.04	0.14
NorESM2-LM	1.85	1.06	0.79	−0.11	−0.28	0.64	0.12	0.06	0.35
UKESM1-0-LL	1.80	1.10	0.70	−0.11	−0.23	0.57	0.06	0.03	0.38
Mean	1.80	1.17	0.63	−0.10	−0.25	0.60	0.09	0.05	0.24
St. dev.	0.11	0.11	0.16	0.01	0.08	0.06	0.09	0.02	0.15

that the stratospheric temperature adjustment to methane was approximately zero, we find a larger stratospheric temperature adjustment for WMGHGs compared to CO$_2$ implying a positive non-CO$_2$ WMGHG stratospheric adjustment, although this cannot be attributed to individual gases.

300   The multi-model mean non-CO$_2$ WMGHG ERF of 1.07 W m^{-2} is close to the 1850–2014 theoretical RF of 1.09 W m^{-2} made up of CH$_4$ (0.55 W m^{-2}) plus N$_2$O (0.17 W m^{-2}) from Etminan et al. (2016), plus halocarbons (0.37 W m^{-2}) using relationships from Myhre et al. (2013).

As for CO$_2$ only forcing, the total adjustment approximately equals the stratospheric temperature adjustment, implying that tropospheric and surface adjustments approximately cancel (table 4) so that the uncertainty in their sum is smaller than for

305   each component individually. The GISS-E2-1-G model does not show the anomalous cooling for tropospheric temperature and water vapour but does show a negative cloud adjustment not seen in other models. For the ISCCP-simulator cloud adjustments, a very similar pattern can be seen from all WMGHGs to CO$_2$-only forcing, with a larger reduction in mid-troposphere fraction leading to a greater positive SW adjustment.

The spread in ERF and stratospheric temperature adjustments is larger for WMGHG than for CO$_2$ forcing alone. One

310   factor may be the inclusion or exclusion of stratospheric chemistry, which affects ozone formation. The effect can be seen by comparing Earth system (ESM) and physical models from the same group: the UKESM1-0-LL ESM (model 13) to the
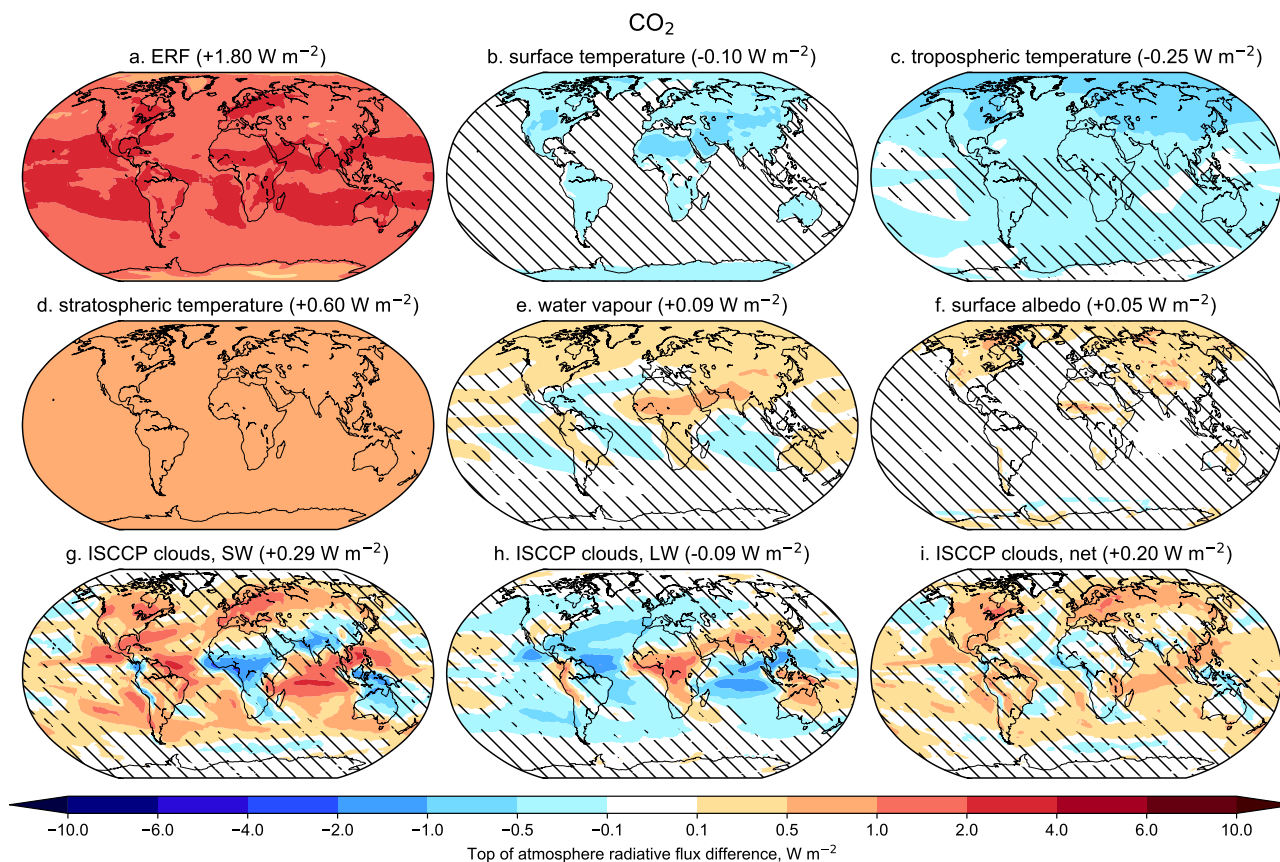
Figure 5. Multi-model mean spatial patterns of (a) effective radiative forcing, (b–f) adjustments and (g–i) cloud contributions to ERF for $1.4 \times CO_2$. Hatched regions are where changes are not significant at the one standard deviation level.

HadGEM3-GC31-LL physical model (model 7), and CNRM-ESM2-1 (model 4) to CNRM-CM6-1 (model 3). The physical models show ERFs around $0.2 \, \text{W m}^{-2}$ greater than the ESMs, a greater IRF, and a smaller stratospheric temperature adjustment. Additionally, for UKESM1-0-LL, large and compensating ERFs from CH_4 ($+0.93 \, \text{W m}^{-2}$) and halocarbons ($-0.33 \, \text{W m}^{-2}$), resulting from interactive chemistry, bring the total WMGHG ERF closer to the no-chemistry ERFs total from HadGEM3-GC31-LL (O'Connor et al., submitted).

The spatial patterns are overall similar to the CO_2 experiment (fig. 6) with a larger magnitude. The tropospheric warming is more robust to all-WMGHG forcing, as GISS-E2-1-G conforms to other models and shows a tropospheric warming.

315

Table 4. As for table 3 but for 1850–2014 well-mixed greenhouse gas forcing.

Model	ERF	IRF	Adj.	ts	ta_tr	ta_st	hus	albedo	cl
CanESM5	2.87	2.13	0.74	−0.15	−0.47	0.74	0.21	0.05	0.35
CESM2	3.03	1.94	1.10	−0.15	−0.44	0.70	0.25	0.12	0.61
CNRM-CM6-1	2.74	1.73	1.01	−0.15	−0.40	1.01	0.17	0.08	0.30
CNRM-ESM2-1	2.51	1.44	1.07	−0.10	−0.38	1.14	0.13	0.08	0.19
GFDL-CM4	3.13	2.34	0.80	−0.13	−0.48	0.56	0.33	0.15	0.37
GISS-E2-1-G	2.89	2.34	0.55	−0.14	−0.38	0.83	0.15	0.13	−0.04
HadGEM3-GC31-LL	3.11	2.11	0.99	−0.15	−0.36	0.75	0.19	0.06	0.50
IPSL-CM6A-LR	2.82	1.81	1.01	−0.13	−0.39	0.83	0.22	0.05	0.44
MIROC6	2.69	2.14	0.54	−0.13	−0.41	0.66	0.19	0.07	0.16
MPI-ESM1-2-LR	2.69	2.00	0.69	−0.14	−0.51	0.79	0.29	0.06	0.19
MRI-ESM2-0	3.03	2.30	0.73	−0.12	−0.46	0.72	0.27	0.05	0.27
NorESM2-LM	2.80	1.93	0.87	−0.14	−0.39	0.74	0.19	0.08	0.38
UKESM1-0-LL	2.94	1.44	1.50	−0.16	−0.38	1.23	0.16	0.05	0.60
Mean	2.87	1.97	0.89	−0.14	−0.42	0.82	0.21	0.08	0.33
St. dev.	0.18	0.29	0.25	0.02	0.05	0.18	0.06	0.03	0.18

5.3 Aerosols

5.3.1 Forcing and adjustments

Present-day aerosol ERF is -1.04 (± 0.23) W m^{-2} from 12 models. We exclude MPI-ESM1.2-LR in this estimate, since it uses prescribed aerosol optical properties and an associated effect on clouds from the simple plumes parameterization (MACv2-SP, Fiedler et al., 2017; Stevens et al., 2017) that will form the separate model inter-comparison of RFMIP-SpAer. The full range of aerosol ERF estimates for 2014 versus 1850 is -0.63 to -1.37 W m^{-2}. This is a narrower range of ERF than similar experiments performed with CMIP5 models for year 1850 and year 2000 forcings (Zelinka et al., 2014), particularly in relation to the lower (more negative) bound of aerosol forcing. Based on the 2000–1850 estimate of -1.17 (± 0.30) W m^{-2} from Zelinka et al. (2014), aerosol forcing in CMIP6 models is less negative than in CMIP5, but this difference again is not significant (p-value 0.26). Some of this multi-model mean difference is likely due to lower emissions of aerosol precursors in 2014 relative to 2000 along with updated historical estimates for CMIP6 (Hoesly et al., 2018; Lamarque et al., 2010), although it is not clear that this explains the reduction in model spread in CMIP6.

Atmospheric adjustments are small in magnitude in the aerosol forcing experiment, but large enough such that there is a noticeable difference between ERF and RF. The small non-cloud adjustments in most models shows that the aerosol forcing is dominated by scattering aerosols (sulfate, organics, and for a limited number of models, nitrates) rather than black carbon
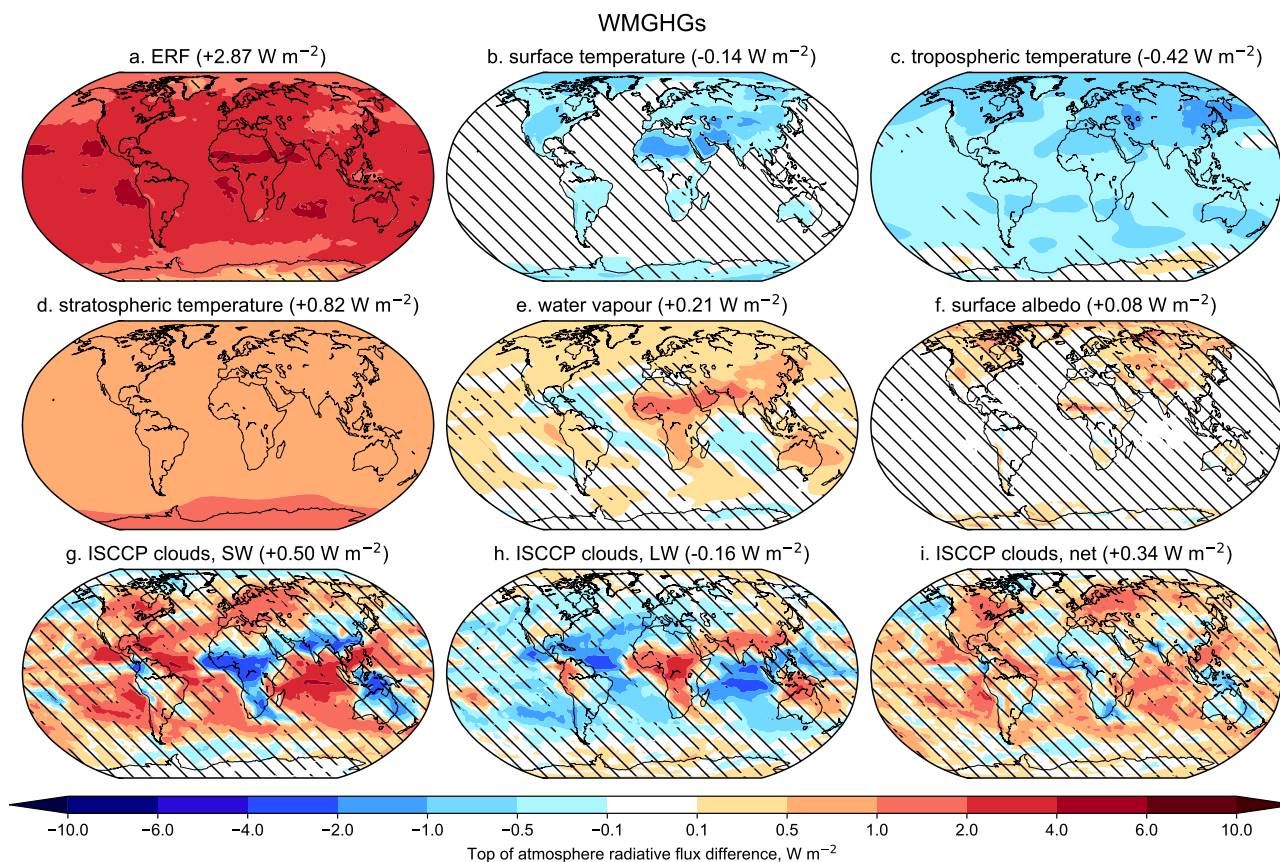
Figure 6. As fig. 5 but for present-day WMGHG forcing.

(Smith et al., 2018). Additionally, in two of the four models that provide the single-forcing BC experiment in AerChemMIP
335   (CNRM-ESM2-1 and UKESM1-0-LL) the overall adjustment is small (Thornhill et al., submitted), in contrast to findings in
PDRMIP models (Smith et al., 2018). In MRI-ESM2-0 (model 11) there are strong tropospheric temperature and cloud changes
to black carbon forcing resulting in a negative adjustment overall (Thornhill et al., submitted).

For aerosol forcing, the aerosol-cloud interactions dominate, with a close to uniform increase in optical thickness at all cloud
heights. As cloud droplet effective radius decreases, cloud albedo, and hence optical thickness, increases. This also implies that
340   absorbing aerosols play only a minor role in most models, as BC induces strong adjustments that cause a general increase in
cloud height in PDRMIP models from an increasing tropospheric stability (Smith et al., 2018; Stjern et al., 2017) for which there
is no evidence in the RFMIP aerosol forcing experiment, although some models do also include aerosol-cloud interactions from
BC. Figure S2 shows ISCCP simulator results for the five PDRMIP experiments from the CMIP5-era HadGEM2-ES model,
where it can be seen that the aerosol forcing experiment is qualitatively more similar to the $5 \times SO_4$ forcing experiment than
345   the $10 \times BC$ experiment in PDRMIP. The increase in cloud albedo leads to a strong negative SW radiative effect that is partially
compensated by LW effects (note that the ISCCP simulator kernel does not distinguish RFaci from adjustments).

Table 5. As for table 3 but for 1850–2014 aerosol forcing.

Model	ERF	IRF	Adj.	ts	ta_tr	ta_st	hus	albedo	cl
CanESM5	−0.85	−0.51	−0.34	0.02	−0.16	−0.10	0.18	0.01	−0.28
CESM2	−1.37	−1.41	0.04	−0.02	−0.00	−0.07	0.10	−0.01	0.03
CNRM-CM6-1	−1.15	−1.22	0.06	0.07	0.15	−0.00	−0.08	−0.06	−0.00
CNRM-ESM2-1	−0.74	−0.78	0.04	0.06	0.10	−0.01	−0.06	−0.02	−0.03
GFDL-CM4	−0.73	−0.56	−0.17	0.05	−0.03	−0.02	0.07	−0.07	−0.17
GISS-E2-1-G	−1.32	−0.45	−0.87	0.06	0.22	−0.03	−0.09	−0.09	−0.94
HadGEM3-GC31-LL	−1.10	−1.03	−0.07	0.05	0.10	0.01	−0.05	−0.04	−0.15
IPSL-CM6A-LR	−0.63	−0.60	−0.03	0.05	0.06	−0.11	0.01	−0.00	−0.03
MIROC6	−1.04	−1.21	0.15	0.06	0.17	0.01	−0.10	−0.03	0.05
MRI-ESM2-0	−1.21	−0.48	−0.72	0.04	−0.24	−0.00	0.17	−0.02	−0.66
NorESM2-LM	−1.21	−1.13	−0.08	0.00	0.03	−0.05	0.02	−0.04	−0.05
UKESM1-0-LL	−1.13	−1.00	−0.13	0.06	0.02	0.00	0.01	−0.05	−0.18
Mean	−1.04	−0.87	−0.18	0.04	0.03	−0.03	0.01	−0.04	−0.20
St. dev.	0.23	0.33	0.30	0.03	0.13	0.04	0.09	0.03	0.29

Unlike for WMGHGs, aerosol forcing adjustments are dominated by cloud effects with only small non-cloud components (table 5). For aerosol forcing, all model years are used, as the stratospheric temperature adjustment is negligible. The spread in values of cloud adjustments is large, and spans positive and negative values. This reconfirms that atmospheric processes in response to aerosol forcing remains one of the largest uncertainties in climate models. There is also a spread in tropospheric temperature and water vapour adjustments with multi-model means near zero, suggesting that some models respond to aerosols with substantial atmospheric warming or cooling.

For many regions, particularly Southern Asia and the Eastern Pacific, the aerosol ERF is driven by large and negative cloud changes (fig. 7). The small adjustment overall and increase in cloud optical thickness for all ISCCP cloud categories suggests this is driven by an increase in cloud condensation nuclei leading to a more negative RFaci. There are some regions such as the Sahara in which a positive ERF arises and not easily explained by any adjustment component. This may be a reduction in mineral dust loading and increase in BC loading, leading to a positive forcing (e.g. as seen in NorESM2-LM, fig. S3).

The total derived cloud adjustment for aerosols is -0.20 W m^{-2}, derived of -0.04 W m^{-2} from SW cloud liquid water path adjustment, -0.15 W m^{-2} from SW cloud fraction change, and -0.02 W m^{-2} from cloud changes in the LW (table S2).

5.3.2 Relationship to climate sensitivity

The increase in the upper bound, and in the overall spread, of equilibrium climate sensitivity (ECS) in the CMIP6 model population compared to CMIP5 is well-documented (Forster et al., 2019; Zelinka et al., accepted). Figure 8 shows the relationships
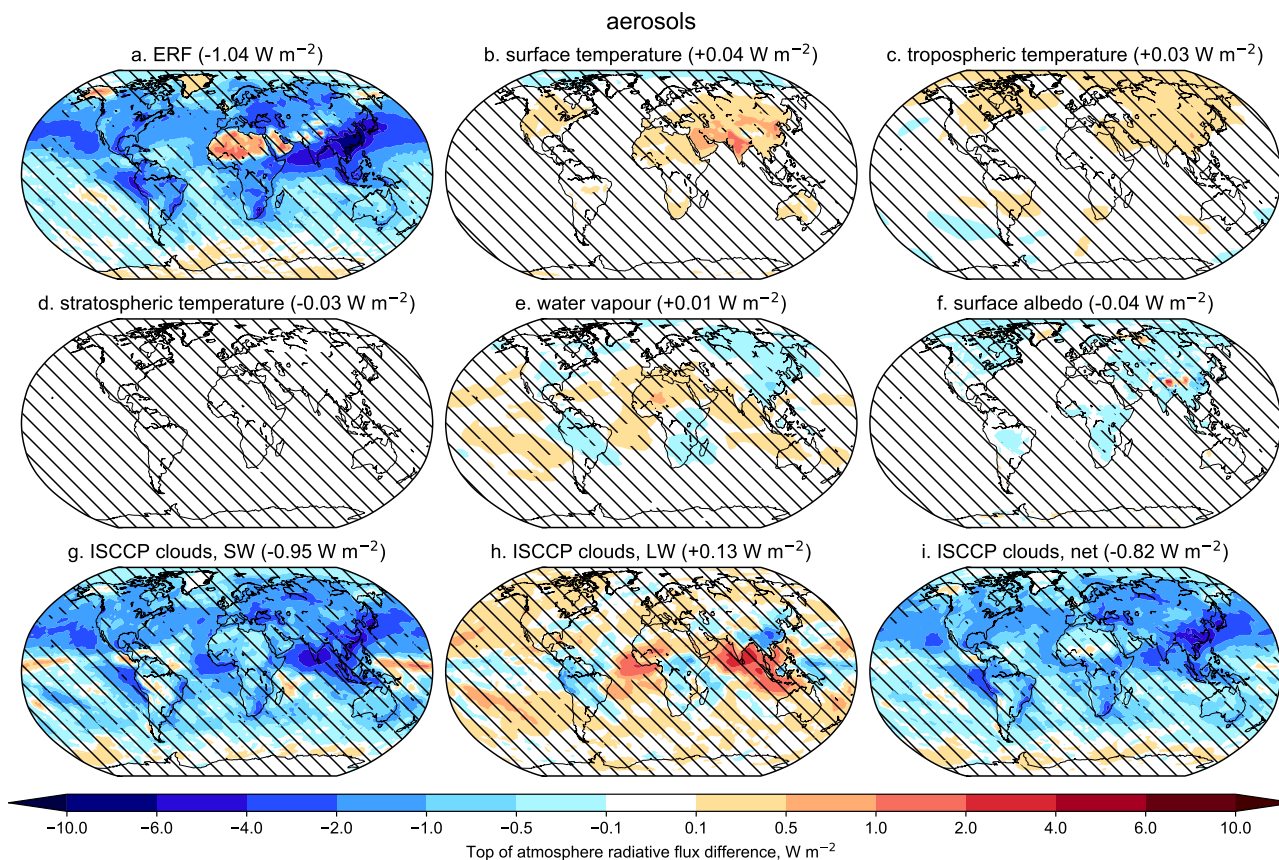
Figure 7. As fig. 5 but for present-day aerosol forcing.

between ECS and transient climate response (TCR) and aerosol ERF in CMIP6, taking ECS and TCR from each model's abrupt4xCO2 and 1pctCO2 CMIP runs respectively. There are weak and non-significant positive correlations between ECS

365 and aerosol forcing ($r = 0.23$) and between TCR and aerosol forcing ($r = 0.30$). This suggests that, as a population, models with high sensitivity are not tuning present-day aerosol forcing to be strong in order to reproduce observed warming: it would be expected that these correlations would be negative if this was the case. In CMIP5 models, aerosol forcing was stronger in models with higher ECS and TCR, but not significantly so (Forster et al., 2013). It may be the case that aerosol forcing over the whole historical transient aerosol forcing is stronger in CMIP6 than in CMIP5, as despite higher climate sensitivity, CMIP6

370 models warm less than CMIP5 models and observations up until 2000 (Flynn and Mauritsen, submitted).

5.3.3 Decomposition of aerosol forcing into aerosol-radiation and aerosol-cloud effects

The approximate partial radiative perturbation (APRP) method (Taylor et al., 2007) can be used to decompose shortwave (SW) aerosol forcing into aerosol-radiation interactions (ERFari), aerosol-cloud interactions (ERFaci), and the surface albedo adjustment (Zelinka et al., 2014). In section 5.3.4 we compare other methods to estimate ERFari and ERFaci. ERFari is the
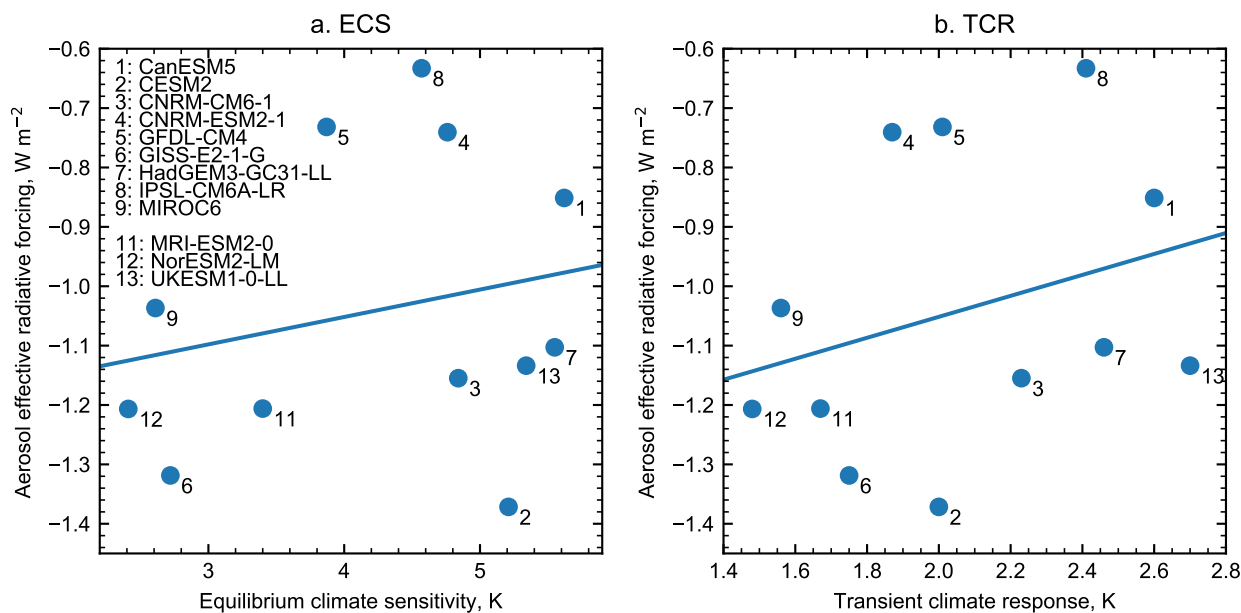
Figure 8. Relationship between (a) ECS and (b) TCR and aerosol ERF in the CMIP6 model ensemble. MPI-ESM1.2-LR (model 10) did not produce the aer, abrupt4xCO2 or 1pctCO2 experiments.

375   component of aerosol forcing that arises from the direct radiative effect of aerosol absorption and scattering (RFari) plus any adjustments (formerly known as the semi-direct effect) arising from perturbations in tropospheric heating rates, humidity, and their consequential effects on where clouds form (Boucher et al., 2013). These adjustments tend to be strong for black carbon but weak for scattering aerosol (Smith et al., 2018; Stjern et al., 2017). ERFaci is composed of any changes in cloud albedo resulting from aerosols acting as cloud condensation nuclei and changing cloud droplet effective radius (RFaci, formerly the

380   first indirect or Twomey effect, Twomey (1977)), plus adjustments relating to cloud lifetime and precipitation efficiency that changes liquid water path and cloud fraction (formerly second indirect or Albrecht effect, Albrecht (1989)). RFaci tends to be strong for sulfate aerosol, but several models also include cloud interactions to other aerosol species, and four models (CESM2, MIROC6, MRI-ESM2-0 and NorESM2-LM) include aerosol interaction on ice clouds. The direct plus Twomey effects (RFari+aci) are treated as the IRF component of aerosol forcing, with the remaining components of ERFari+aci as

385   adjustments (Boucher et al., 2013).

     There is no equalivent longwave (LW) method to APRP, so we take the approach of Zelinka et al. (2014) and use the cloud radiative effect to decompose LW ERF into ERFari and ERFaci. The advantages of these techniques are that they only require standard CMIP output, and all participating models can provide estimates. Results are displayed in table 6 and shown in fig. 9.

     The total ERFari+aci from the APRP method is -1.05 ($\pm$ 0.22) W m^{-2}, agreeing very well with the ERF estimate of

390   -1.04 (± 0.23) W m^{-2}. ERFari+aci is approximately 20% from ERFari and 80% from ERFaci, and is comprised of a SW contribution of -1.33 W m^{-2} offset by a LW contribution of $+0.28$ W m^{-2}. The model spread in both the SW and LW

Table 6. Contribution of the components of 1850–2014 effective radiative forcing from aerosols. ARI: ERF due to aerosol-radiation interactions; ACI: ERF due to aerosol-cloud interactions; scat=scattering; abs=absorption; amt=cloud amount.

Model	SW								LW			Net		
	ARI			ACI				ARI+ACI	ARI	ACI	ARI+ACI	ARI	ACI	ARI+ACI
	scat	abs	sum	scat	abs	amt	sum							
CanESM5	−0.60	0.52	−0.08	−0.88	0.06	−0.14	−0.96	−1.04	0.06	−0.08	−0.02	−0.02	−1.04	−1.06
CESM2	−0.26	0.35	0.09	−1.70	0.03	−0.01	−1.68	−1.58	0.05	0.10	0.16	0.15	−1.57	−1.43
CNRM-CM6-1	−0.61	0.20	−0.41	−0.77	−0.05	0.05	−0.77	−1.18	0.15	−0.05	0.09	−0.26	−0.82	−1.08
CNRM-ESM2-1	−0.42	0.18	−0.24	−0.52	−0.04	−0.03	−0.59	−0.83	0.10	−0.02	0.08	−0.14	−0.61	−0.75
GFDL-CM4	−0.65	0.41	−0.24	−0.54	0.00	−0.09	−0.62	−0.86	0.13	−0.06	0.07	−0.11	−0.68	−0.80
GISS-E2-1-G	−0.91	0.19	−0.72	0.06	0.01	−0.94	−0.87	−1.59	0.19	0.10	0.29	−0.52	−0.78	−1.30
HadGEM3-GC31-LL	−0.77	0.30	−0.47	−0.75	−0.01	−0.07	−0.83	−1.30	0.20	−0.00	0.19	−0.28	−0.83	−1.11
IPSL-CM6A-LR	−0.60	0.17	−0.43	−0.26	−0.01	0.06	−0.22	−0.65	0.06	−0.07	−0.01	−0.37	−0.28	−0.65
MIROC6	−0.48	0.09	−0.39	−1.04	−0.06	−0.01	−1.12	−1.51	0.18	0.38	0.57	−0.21	−0.73	−0.94
MRI-ESM2-0	−0.70	0.19	−0.51	−1.71	−0.09	−0.38	−2.18	−2.69	0.05	1.47	1.52	−0.46	−0.71	−1.17
NorESM2-LM	−0.42	0.21	−0.21	−1.07	−0.00	−0.10	−1.17	−1.38	0.07	0.14	0.21	−0.14	−1.03	−1.17
UKESM1-0-LL	−0.72	0.34	−0.39	−0.82	−0.00	−0.10	−0.92	−1.31	0.19	−0.04	0.15	−0.20	−0.97	−1.16
Mean	−0.59	0.26	−0.33	−0.83	−0.01	−0.15	−0.99	−1.33	0.12	0.16	0.27	−0.21	−0.84	−1.05
St. dev.	0.17	0.12	0.20	0.49	0.04	0.26	0.49	0.50	0.06	0.42	0.40	0.18	0.30	0.22
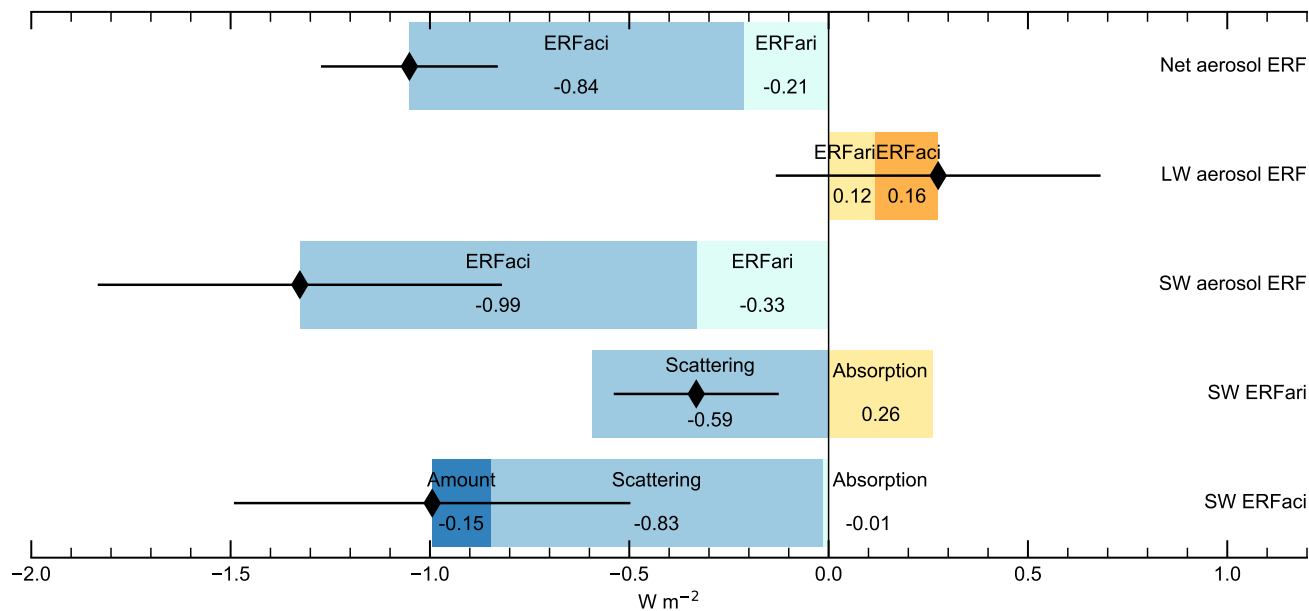
Figure 9. Components of the aerosol forcing diagnosed from the Approximate Partial Radiative Perturbation (for SW aerosol components) and from the cloud radiative effect (for LW components). Black diamonds represent multi-model means, black bars show one standard deviation.

individual components is larger than for the net forcing. This is driven by the four models that include ice cloud interactions that show positive LW ERFaci offset by strong negative SW ERFaci. MRI-ESM2.0 in particular has a very large positive LW ERFaci of $+1.47$ W m^{-2}, which comes from ice cloud nucleation by black carbon aerosols with temperature below $-38°$C in high-level clouds in the tropics. For the SW component the ERFari/ERFaci split is 25% to 75%.

Multi-model mean SW ERFari is -0.33 W m^{-2}, comprised of an absorption of $+0.26$ W m^{-2} offset by scattering of -0.59 W m^{-2}. The SW ERFaci is -0.99 W m^{-2}, made up of scattering (-0.83 W m^{-2}), absorption (-0.01 W m^{-2}) and cloud fraction change (-0.15 W m^{-2}).

5.3.4 Comparison of ERFari and ERFaci methods

Six models also archived radiation diagnostics from aerosol-free radiation calls (the double call method) as recommended by Ghan (2013). The aerosol forcing is estimated as
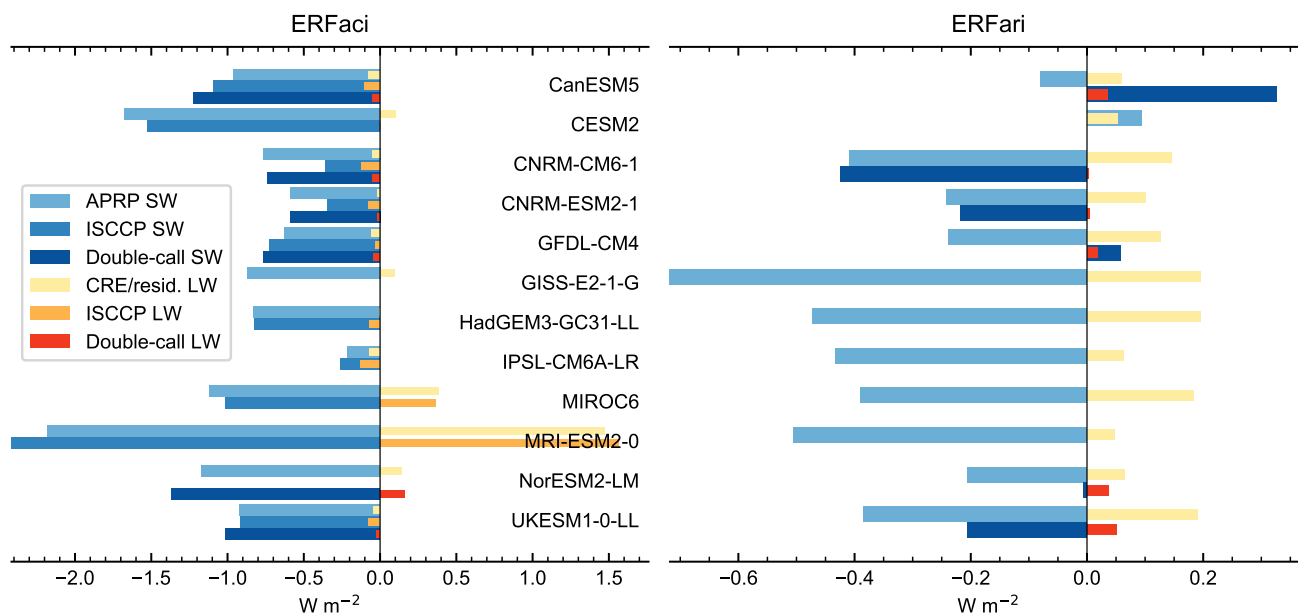
Figure 10. Comparison of methods to estimate ERFaci and ERFari from the aerosol experiment. CRE/resid. is the LW cloud radiative effect for ERFaci and the difference of LW ERF and CRE for ERFari. Not all methods are available in all models.

$$\text{ERFariSW} \quad = \quad -\Delta\text{rsut} - (-\Delta\text{rsutaf}) \tag{6}$$

$$\text{ERFaciSW} \quad = \quad -\Delta\text{rsutaf} - (-\Delta\text{rsutcsaf}) \tag{7}$$

$$\text{ERFariLW} \quad = \quad -\Delta\text{rlut} - (-\Delta\text{rlutaf}) \tag{8}$$

$$\text{ERFaciLW} \quad = \quad -\Delta\text{rlutaf} - (-\Delta\text{rlutcsaf}) \tag{9}$$

with variable names corresponding to CMIP6 TOA upwelling radiation diagnostics (r<l,s>ut[cs][af]; l=longwave, s=shortwave, cs = clear-sky, af=aerosol-free) and Δ representing the present-day minus pre-industrial difference.

Figure 10 shows different methods of estimating ERFaci and ERFari from the aerosol forcing experiment. For ERFaci in both the SW and LW, different methods provide similar estimates. For ERFari, the APRP and double-call methods sometimes disagree, however the ERFari is smaller than ERFaci. Additionally, it can also be noted that the LW ERFari+aci from the double-call method does not always equal the total ERF and may introduce a residual. For the CRE residual method the implied ERFari+aci equals the true ERF by definition, but some non-cloud rapid adjustments may be aliased into the total.

5.4 Land-use change

Land use ERF is small and not significant at -0.08 (± 0.14) W m^{-2}. Forcing and adjustments are difficult to distinguish from
415 zero and it is unlikely that this forcing played a large role historically for global mean impacts. In 11 of 12 models (land cover
change is not provided in CNRM-CM6.1, so this experiment was not run), land-use ERF is negative, and the multi-model
mean and standard deviation is affected by a relatively large positive forcing in the NorESM2-LM model, whereas all other
models show a negative ERF. In fig. S3g we show that this is due to cloud adjustments in this model. This is a consequence of
interactive isoprene and monoterpene specified from the land surface changes, causing a reduction in organic matter, reducing
420 cloud condensation nuclei and increasing SW cloud adjustment (unlike for the aerosol forcing experiment, the Twomey effect
in response to a land use forcing is treated as an adjustment and not a forcing, because anthropogenic aerosol emissions are not
perturbed). In other models, where the ERF is small and negative, it should also be borne in mind that internal variability may
make it more difficult to isolate the forcing signal from the noise in free-running simulations (Forster et al., 2016), although the
multi-model mean is likely to be more robust than individual model results. This experiment was partly motivated by a large
425 land use forcing of -0.4 W m^{-2} in the CMIP5 HadGEM2-ES model (Andrews et al., 2017); the successor UKESM1-0-LL
model also shows a relatively strong land-use forcing of -0.30 W m^{-2}, although the physical model from the same group
(HadGEM3-GC31-LL) does not show such a strong land use forcing (-0.11 W m^{-2}).

The radiative forcing from land use change is driven by the resulting change in surface albedo. For example, deforestation
for agricultural use converts relatively dark forest cover to brighter cropland, exerting a negative forcing (Betts, 2000, 2001).
430 The surface albedo kernel-derived flux change is taken to be the IRF. It is not a perfect measure as it includes changes in snow
and ice cover over land, and any biophysical response, as both changes in land surface temperatures and surface properties can
affect snow cover. However, the land surface temperature change is very small in the land-use experiment, evidenced by the
small land surface temperature adjustment in fig. 3. Changes in surface properties such as how snow cover settles over different
land types and the biophysical response is not easy to discern from model output. Again, all available model years are used
435 because stratospheric temperature adjustment does not play a large role.

The spatial pattern of land-use forcing and adjustments (fig. 11) is generally not significant in many parts of the world due to
the small size of the forcing. The exception to this is water vapour and SW cloud adjustments over the Amazon; deforestation
from pre-industrial to present-day is likely to have reduced evapotranspiration from vegetation, reducing tropospheric humidity
and low level cloud cover. These spatial patterns are also coincident with a decrease in organic carbon loading in NorESM2-LM
440 (fig. S3).

5.5 Anthropogenic total

The total anthropogenic ERF for 1850–2014 stands at 1.97 ($\pm$ 0.26) W m^{-2} (12 models; MPI-ESM2-0 did not run this
experiment; CNRM-CM6-1 is included but did not include effects of land use change). Inter-model spread is larger, both in
relative and absolute terms, in the total anthropogenic forcing than it is for any of its individual components, suggesting that
445 individual models respond very differently to the same combinations of forcing. In the absence of non-linearities between

Table 7. As for table 3 but for 1850–2014 land-use forcing.

Model	ERF	IRF	Adj.	ts	ta_tr	ta_st	hus	cl
CanESM5	−0.08	−0.10	0.03	0.02	−0.02	0.01	−0.00	0.02
CESM2	−0.04	−0.08	0.05	−0.01	0.03	0.00	0.01	0.03
CNRM-ESM2-1	−0.07	−0.08	0.02	0.01	−0.02	−0.01	0.04	−0.00
GFDL-CM4	−0.33	−0.42	0.09	−0.04	0.09	0.00	−0.06	0.08
GISS-E2-1-G	−0.00	0.02	−0.02	−0.02	−0.02	0.01	0.02	−0.01
HadGEM3-GC31-LL	−0.11	−0.16	0.06	0.01	0.10	0.01	−0.05	−0.02
IPSL-CM6A-LR	−0.05	−0.11	0.07	−0.01	0.02	0.00	−0.01	0.07
MIROC6	−0.03	−0.10	0.08	−0.01	0.04	0.00	−0.04	0.10
MPI-ESM1-2-LR	−0.10	−0.01	−0.09	−0.01	0.01	0.01	−0.01	−0.10
MRI-ESM2-0	−0.17	−0.33	0.16	0.00	0.08	−0.00	−0.08	0.16
NorESM2-LM	0.26	−0.01	0.27	0.01	0.01	0.00	0.00	0.25
UKESM1-0-LL	−0.30	−0.28	−0.01	0.02	0.08	−0.01	−0.04	−0.06
Mean	−0.08	−0.14	0.06	−0.00	0.03	0.00	−0.02	0.04
St. dev.	0.14	0.13	0.09	0.02	0.04	0.01	0.03	0.09

forcing components, the residual ERF of $+0.17$ W m^{-2} from the land-use, aerosol and WMGHG components compared to the total anthropogenic would mostly be comprised of ozone forcing, although the sum of individual forcings does not necessarily equal the total forcing in some models (Thornhill et al., submitted; O'Connor et al., submitted). As for the aerosol forcing experiment, there is no significant correlation between total anthropogenic forcing and ECS or TCR.

450   The total anthropogenic forcing shows the offsetting influences of the greenhouse gas and aerosol forcing components on the ERF, IRF and adjustments. The total anthropogenic ISCCP-simulator cloud changes are also a combination of the WMGHG and aerosol contributions, with the net effect being dominated by aerosol. For non-cloud adjustments the combination of strong positive adjustments from the greenhouse gas forcing with a small negative adjustment from the aerosol forcing results in an adjustment that is of comparable magnitude to the IRF. The exception is the GISS-E2-1-G model that has a very strong negative

455 cloud adjustment, driven by a large increase in cloud fraction in the aerosol experiment (table 6). Additionally, stratospheric adjustment is stronger for total anthropogenic forcing than for WMGHGs alone, suggesting a role for tropospheric ozone forcing in contributing to this adjustment.

     The pattern of anthropogenic forcing is spatially inhomogeneous; positive where aerosol forcing is weak, and negative where localised aerosol-cloud effects dominate (fig. 12). The influence of WMGHG forcing on temperature and water vapour

460 adjustments, and of aerosol forcing on the cloud response, is evident.
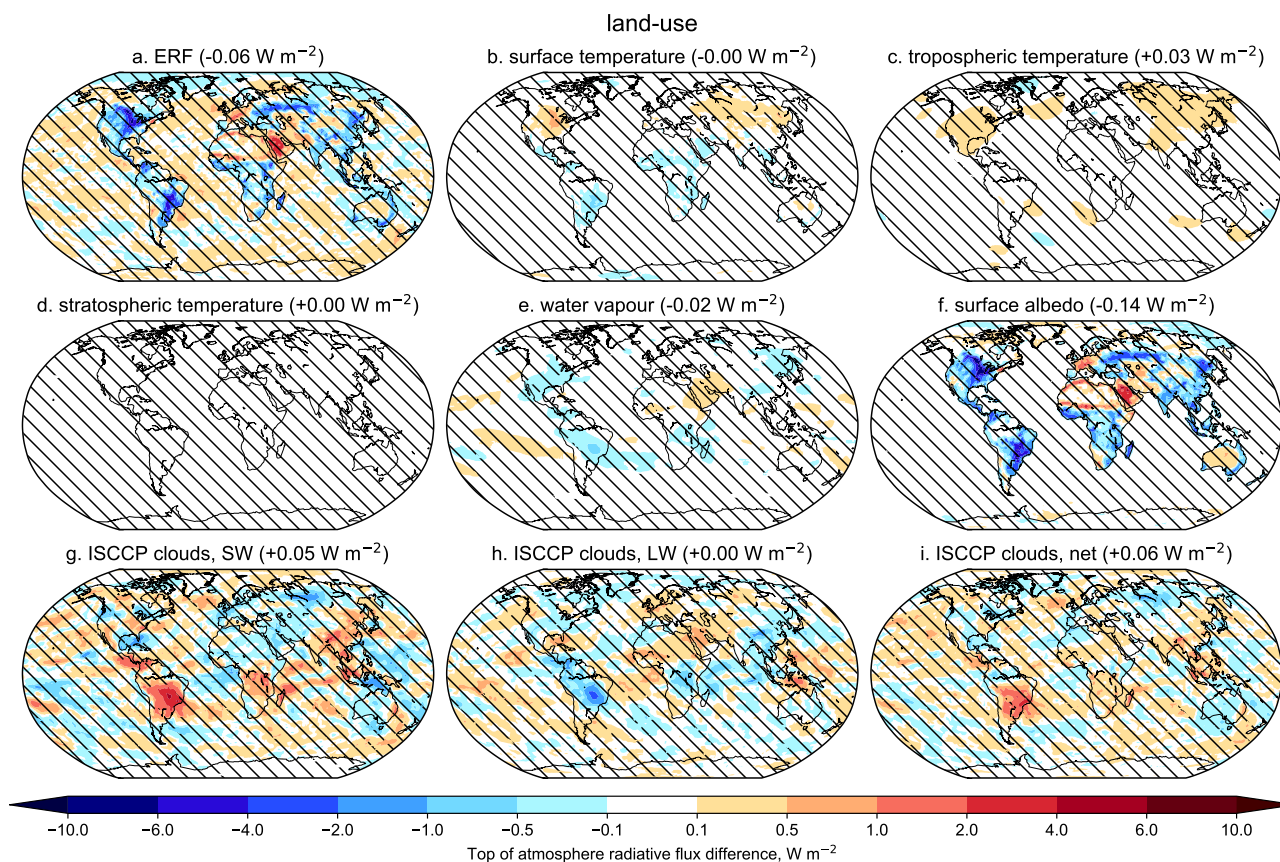
Figure 11. As fig. 5 but for present-day land use forcing. Subplot (f) represents the IRF in this experiment.

6 Conclusions

Effective radiative forcing is the driving process behind long-term changes in global mean surface temperature. As ERF is now preferred to RF, climate models are the best tools we have to determine the heating impacts of various species on the Earth atmosphere system.

From CMIP5 to CMIP6, both CO_2 and aerosol forcing has become more consistent across the population of models. Multi-model mean CO_2 and all-WMGHG ERF estimates agree very well with RF estimates from Etminan et al. (2016) using a line-by-line radiative transfer model (sections 5.1 and 5.2). A comprehensive review of aerosol forcing placed the 16–84% uncertainty range in present-day aerosol ERF at -1.60 to -0.65 W m^{-2} (Bellouin et al., in press). Results from CMIP6 models show a smaller range of -1.27 to -0.81 W m^{-2} (one standard deviation, equivalent to 16–84% range for a Gaussian distribution), though more models may submit results to CMIP6 that would widen this range. Present-day aerosol forcing does not explain the increase in the range of ECS in CMIP6 models, particularly the upper bound.

Table 8. As for table 3 but for 1850–2014 anthropogenic forcing.

Model	ERF	IRF	Adj.	ts	ta_tr	ta_st	hus	albedo	cl
CanESM5	2.37	1.82	0.55	−0.14	−0.70	0.87	0.45	0.03	0.04
CESM2	2.05	0.68	1.38	−0.17	−0.48	0.95	0.44	0.01	0.63
CNRM-CM6-1	1.61	0.55	1.06	−0.07	−0.22	1.01	0.07	0.01	0.26
CNRM-ESM2-1	1.66	0.66	1.01	−0.04	−0.32	1.11	0.16	−0.03	0.13
GFDL-CM4	2.34	2.13	0.21	−0.11	−0.44	0.69	0.31	−0.36	0.13
GISS-E2-1-G	1.93	1.79	0.14	−0.08	−0.14	0.99	0.13	0.13	−0.89
HadGEM3-GC31-LL	1.81	0.98	0.83	−0.09	−0.26	0.97	0.13	−0.20	0.29
IPSL-CM6A-LR	2.32	1.36	0.96	−0.11	−0.40	0.94	0.28	−0.08	0.33
MIROC6	1.80	1.05	0.74	−0.10	−0.29	0.87	0.14	−0.02	0.14
MRI-ESM2-0	1.95	1.72	0.23	−0.10	−0.59	0.93	0.44	−0.28	−0.17
NorESM2-LM	2.06	1.09	0.97	−0.14	−0.49	0.99	0.31	−0.05	0.36
UKESM1-0-LL	1.71	0.55	1.16	−0.05	−0.25	1.22	0.12	−0.28	0.40
Mean	1.97	1.20	0.77	−0.10	−0.38	0.96	0.25	−0.09	0.14
St. dev.	0.26	0.53	0.39	0.04	0.16	0.12	0.13	0.14	0.36

We determine a multi-model mean anthropogenic ERF of 1.97 ($\pm$0.26) W m^{-2} for 1850–2014. This is less than the anthropogenic ERF in AR5 for 1850–2011 of 2.24 W m^{-2} (although with large uncertainty), and extrapolating trends forward would suggest an anthropogenic ERF of around 2.4 W m^{-2} from AR5 for 1850–2014. The two main reasons for this difference are a stronger negative aerosol forcing in CMIP6 compared to the AR5 assessment (−1.04 W m^{-2} in CMIP6 for 1850–2014 versus −0.72 W m^{-2} in AR5 for 1850–2011), and a weaker ozone forcing (+0.17 W m^{-2} versus +0.31 W m^{-2}), if residual anthropogenic forcing is attributed to ozone.

Forcing adjustments produce insight into the atmospheric mechanisms that contribute to ERF. Warming of the troposphere results in a negative adjustment due to the increase in outgoing LW radiation, and increasing water vapour counteracts this effect partially by its role as a greenhouse gas. With one exception, all models agree on tropospheric warming and moistening for WMGHG and all-anthropogenic forcing. These tropospheric adjustments are small for aerosol forcing but models do not agree on the sign of the change. Cloud adjustments remain the largest uncertainty in the forcing component in climate models, as well as in the feedback and climate response (Zelinka et al., accepted), and exhibit a wide range of behaviour to both greenhouse gas and aerosol forcing. Constraining cloud responses to both forcing and climate response should therefore continue to be a priority.
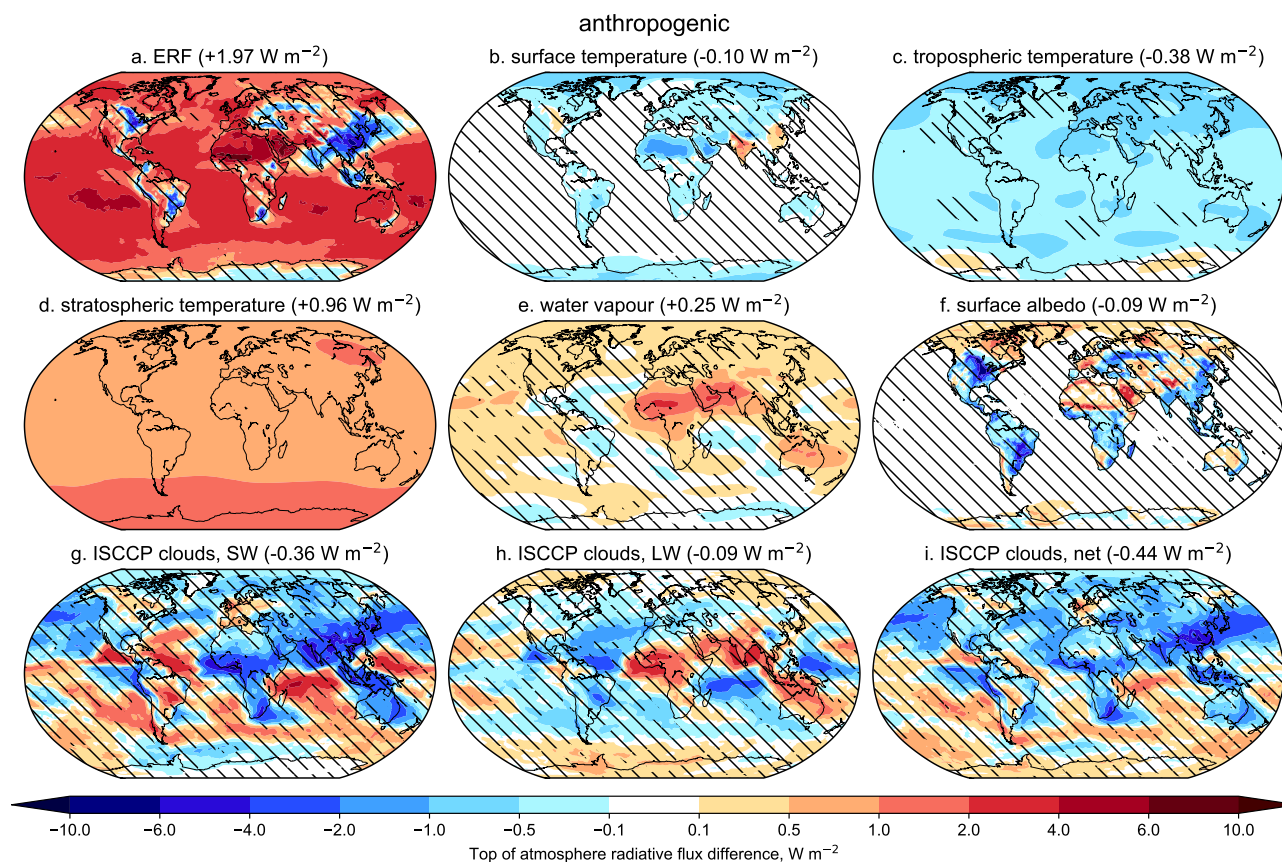
Figure 12. As fig. 5 but for present-day anthropogenic forcing.

Data availability. RFMIP model data used in this study is freely available from the CMIP6 repository on the Earth System Grid Foundation
nodes (https://esgf-node.llnl.gov/search/cmip6/).The HadGEM3-GA7.1 kernels are available at https://doi.org/10.5281/zenodo.3594673.

Author contributions. C.J.S. co-ordinated the project, analysed the data and led the writing of the manuscript. R.J.K. produced adjustment
calculations using radiative kernels. G.M. provided adjustment calculations using offline radiation simulations. K.A. provided model esti-
490   mates of effective radiative forcing and equilibrium climate sensitivity. W.C. provided analysis of different definitions of effective radiative
forcing. R.P. and P.M.F. oversaw the RFMIP-ERF project in coordination with the World Climate Research Programme under the CMIP6
protocol. All other authors ran models and published results on the Earth System Grid Foundation, without which this work would not have
been possible. All authors contributed to the writing and review.

Competing interests. The authors declare no competing interests.

495 *Disclaimer.* TEXT

Acknowledgements. We thank Ed Gryspeerdt, Mark Zelinka, and the participants and hosts of the Tri-MIP-athlon consortium meetings in Reading 2018 and Princeton 2019 for fruitful discussions. We acknowledge the World Climate Research Programme, which, through its Working Group on Coupled Modelling, coordinated and promoted CMIP6. We thank the climate modeling groups for producing and making available their model output, the Earth System Grid Federation (ESGF) for archiving the data and providing access, and the multiple funding agencies who support CMIP6 and ESGF.

500 C.J.S. and P.M.F. were supported by the European Union's Horizon 2020 research and innovation programme under grant agreement No 820829 (CONSTRAIN project). R.J.K. is supported by an appointment to the NASA Postdoctoral Program at NASA Goddard Space Flight Center. RP was supported by the US Department of Energy's Office of Biological and Environmental Research under grant 7457436 from Lawrence Berkeley National Lab. T.A., F.M.O'C., E.R., and A.W. were supported by the Met Office Hadley Centre Climate Programme funded by BEIS and Defra and the Newton Fund through the Met Office Climate Science for Service Partnership Brazil (CSSP Brazil).

505 F.M.O'C. also acknowledges support from the EU Horizon 2020 Research Programme CRESCENDO project, grant agreement number 641816. A.K. and D.O. were supported by the Research Council of Norway (grant nos. 229771, 285003, and 285013), by Notur/NorStore (NN2345K and NS2345K), and through EU H2020 grant no. 280060. H.S. was supported by TOUGOU (MEXT, Japan). The MIROC6 simulations were performed using the Earth Simulator at JAMSTEC and the NEC SX at NIES. The CMIP6 project at IPSL used the

510 HPC resources of TGCC under the allocations 2017-R0040110492 and 2018-R0040110492 (project gencmip6) provided by GENCI (Grand Équipement National de Calcul Intensif). The CESM project is supported primarily by the National Science Foundation. Part of this material is based upon work supported by the National Center for Atmospheric Research, which is a major facility sponsored by the National Science Foundation under Cooperative Agreement No. 1852977.

References

515 Albrecht, B. A.: Aerosols, cloud microphysics, and fractional cloudiness, Science, 245, 1227–1231, 1989.

Allen, R., Amiri-Farahani, A., Lamarque, J.-F., Smith, C., Shindell, D., Hassan, T., and Chung, C.: npj Climate and Atmospheric Science, 2, https://doi.org/10.1038/s41612-019-0073-9, 2019.

Andrews, T., Gregory, J. M., Webb, M. J., and Taylor, K. E.: Forcing, feedbacks and climate sensitivity in CMIP5 coupled atmosphere-ocean climate models, Geophys. Res. Lett., 39, L09 712, https://doi.org/10.1029/2012GL051607, 2012.

520 Andrews, T., Betts, R. A., Booth, B. B. B., Jones, C. D., and Jones, G. S.: Effective radiative forcing from historical land use change, Clim. Dynam., 48, 3489–3505, https://doi.org/10.1007/s00382-016-3280-7, 2017.

Andrews, T., Andrews, M. B., Bodas-Salcedo, A., Jones, G. S., Kuhlbrodt, T., Manners, J., Menary, M. B., Ridley, J., Ringer, M. A., Sellar, A. A., Senior, C. A., and Tang, Y.: Forcings, Feedbacks, and Climate Sensitivity in HadGEM3-GC3.1 and UKESM1, J. Adv. Model. Earth Sy., 11, https://doi.org/10.1029/2019MS001866, 2019.

525 Armour, K.: Energy budget constraints on climate sensitivity in light of inconstant climate feedbacks, Nat. Clim. Change, 7, 331–335, https://doi.org/10.1038/nclimate3278, 2017.

Bellouin, N., Quaas, J., Gryspeerdt, E., Kinne, S., Stier, P., Watson-Parris, D., Boucher, O., Carslaw, K., Christensen, M., Daniau, A.-L., Dufresne, J.-L., Feingold, G., Fiedler, S., Forster, P., Gettelman, A., Haywood, J., Lohmann, U., Malavelle, F., Mauritsen, T., Mc-Coy, D., Myhre, G., Mülmenstädt, J., Neubauer, D., Possner, A., Rugenstein, M., Sato, Y., Schulz, M., Schwartz, S., Sourdeval, O.,
530 Storelvmo, T., Toll, V., Winker, D., and Stevens, B.: Bounding global aerosol radiative forcing of climate change, Rev. Geophys., https://doi.org/10.1029/2019RG000660, in press.

Bellouin, N., Davies, W., Shine, K., Quaas, J., Muelmenstaedt, J., Block, K., Forster, P., Smith, C., Lee, L., Regayre, L., Brasseur, G., Sudarchikova, N., Bouarar, I., Boucher, O., and Myhre, G.: Radiative forcing of climate change from the Copernicus reanalysis of atmospheric composition, Earth Syst. Sci. Data, submitted.

535 Betts, R.: Offset of the potential carbon sink from boreal forestation by decreases in surface albedo, Nature, 408, 187–190, https://doi.org/10.1038/35041545, 2000.

Betts, R. A.: Biogeophysical impacts of land use on present-day climate: near-surface temperature change and radiative forcing, Atmos. Sci. Lett., 2, 39–51, https://doi.org/10.1006/asle.2001.0037, https://rmets.onlinelibrary.wiley.com/doi/abs/10.1006/asle.2001.0037, 2001.

Boucher, O., Randall, D., Artaxo, P., Bretherton, C., Feingold, G., Forster, P., Kerminen, V.-M., Kondo, Y., Liao, H., Lohmann, U., Rasch,
540 P., Satheesh, S., Sherwood, S., Stevens, B., and Zhang, X.: Clouds and Aerosols, in: Climate Change 2013: The Physical Science Basis. Contribution of Working Group I to the Fifth Assessment Report of the Intergovernmental Panel on Climate Change, edited by Stocker, T., Qin, D., Plattner, G.-K., Tignor, M., Allen, S., Boschung, J., Nauels, A., Xia, Y., Bex, V., and Midgley, P., pp. 571–658, Cambridge University Press, Cambridge, United Kingdom and New York, NY, USA, 2013.

Boucher, O., Servonnat, J., Albright, A. L., Aumont, O., Balkanski, Y., Bastrikov, V., Bekki, S., Bonnet, R., Bony, S., Bopp, L., Braconnot, P.,
545 Brockmann, P., Cadule, P., Caubel, A., Cheruy, F., Cozic, A., Cugnet, D., D'Andrea, F., Davini, P., de Lavergne, C., Denvil, S., Deshayes, J., Devilliers, M., Ducharne, A., Dufresne, J.-L., Dupont, E., Éthé, C., Fairhead, L., Falletti, L., Foujols, M.-A., Gardoll, S., Gastineau, G., Ghattas, J., Grandpeix, J.-Y., Guenet, B., Guez, L., Guilyardi, E., Guimberteau, M., Hauglustaine, D., Hourdin, F., Idelkadi, A., Joussaume, S., Kageyama, M., Khodri, M., Krinner, G., Lebas, N., Levavasseur, G., Lévy, C., Li, L., Lott, F., Lurton, T., Luyssaert, S., Madec, G., Madeleine, J.-B., Maignan, F., Marchand, M., Marti, O., Mellul, L., Meurdesoif, Y., Mignot, J., Musat, I., Ottlé, C., Peylin, P., Planton,
550 Y., Polcher, J., Rio, C., Rousset, C., Sepulchre, P., Sima, A., Swingedouw, D., Thiéblemont, R., Traoré, A.-K., Vancoppenolle, M., Vial,

J., Vialard, J., Viovy, N., and Vuichard, N.: Presentation and evaluation of the IPSL-CM6A-LR climate model, J. Adv. Model. Earth Sy., submitted.

Caballero, R. and Huber, M.: State-dependent climate sensitivity in past warm climates and its implications for future climate projections, P. Natl. Acad. Sci. USA, 110, 14 162–14 167, https://doi.org/10.1073/pnas.1303365110, 2013.

555 Chung, E.-S. and Soden, B. J.: An assessment of methods for computing radiative forcing in climate models, Env. Res. Lett., 10, 074 004, https://doi.org/10.1088/1748-9326/10/7/074004, https://doi.org/10.1088%2F1748-9326%2F10%2F7%2F074004, 2015.

Collins, W. J., Lamarque, J.-F., Schulz, M., Boucher, O., Eyring, V., Hegglin, M. I., Maycock, A., Myhre, G., Prather, M., Shindell, D., and Smith, S. J.: AerChemMIP: quantifying the effects of chemistry and aerosols in CMIP6, Geosci. Model Dev., 10, 585–607, https://doi.org/10.5194/gmd-10-585-2017, https://www.geosci-model-dev.net/10/585/2017/, 2017.

560 Colman, R. and McAvaney, B.: Climate feedbacks under a very broad range of forcing, Geophysical Research Letters, 36, https://doi.org/10.1029/2008GL036268, 2009.

Copernicus Climate Change Service: ERA5: Fifth generation of ECMWF atmospheric reanalyses of the global climate, https://cds.climate.copernicus.eu/cdsapp#!/home, accessed 28 October 2019, 2017.

Danabasoglu, G., Lamarque, J. F., Bachmeister, J., Bailey, D. A., DuVivier, A. K., Edwards, J., Emmons, L. K., Fasullo, J., Garcia, R.,
565 Gettelman, A., Hannay, C., Holland, M. M., Large, W. G., Lawrence, D. M., Lenaerts, J. T. M., Lindsay, K., Lipscomb, W. H., Mills, M. J., Neale, R., Oleson, K. W., Otto-Bliesner, B., Phillips, A. S., Sacks, W., Tilmes, S., van Kampenhout, L., Vertenstein, M., Bertini, A., Dennis, J., Deser, C., Fischer, C., Fox-Kember, B., Kay, J. E., Kinnison, D., Kushner, P. J., Long, M. C., Mickelson, S., Moore, J. K., Nienhouse, E., Polvani, L., Rasch, P. J., and Strand, W. G.: The Community Earth System Model version 2 (CESM2), J. Adv. Model. Earth Sy., submitted.

570 Edwards, J. M. and Slingo, A.: Studies with a flexible new radiation code. I: Choosing a configuration for a large-scale model, Q. J. Roy. Meteor. Soc., 122, 689–719, https://doi.org/10.1002/qj.49712253107, 1996.

Etminan, M., Myhre, G., Highwood, E. J., and Shine, K. P.: Radiative forcing of carbon dioxide, methane, and nitrous oxide: A significant revision of the methane radiative forcing, Geophys. Res. Lett., 43, 12,614–12,623, https://doi.org/10.1002/2016GL071930, 2016GL071930, 2016.

575 Eyring, V., Bony, S., Meehl, G. A., Senior, C. A., Stevens, B., Stouffer, R. J., and Taylor, K. E.: Overview of the Coupled Model Intercomparison Project Phase 6 (CMIP6) experimental design and organization, Geosci. Model Dev., 9, 1937–1958, https://doi.org/10.5194/gmd-9-1937-2016, https://www.geosci-model-dev.net/9/1937/2016/, 2016.

Fiedler, S., Stevens, B., and Mauritsen, T.: On the sensitivity of anthropogenic aerosol forcing to model-internal variability and parameterizing a Twomey effect, J. Adv. Model. Earth Sy., 9, 1325–1341, https://doi.org/10.1002/2017MS000932, 2017.

580 Flynn, C. M. and Mauritsen, T.: On the Climate Sensitivity and Historical Warming Evolution in Recent Coupled Model Ensembles, Atmospheric Chemistry and Physics, submitted.

Forster, P., Richardson, T., Maycock, A., Smith, C., Samset, B., Myhre, G., Andrews, T., Pincus, R., and Schulz, M.: Recommendations for diagnosing effective radiative forcing from climate models from CMIP6, J. Geophys. Res., 121, 12 460–12 475, https://doi.org/10.1002/2016JD025320, 2016.

585 Forster, P., Maycock, A., McKenna, C., and Smith, C.: Latest climate models confirm need for urgent mitigation, Nat. Clim. Change, 2019.

Forster, P. M., Andrews, T., Good, P., Gregory, J. M., Jackson, L. S., and Zelinka, M.: Evaluating adjusted forcing and model spread for historical and future scenarios in the CMIP5 generation of climate models, J. Geophys. Res.-Atmos., 118, 1139–1150, https://doi.org/10.1002/jgrd.50174, 2013.

Forster, P. M. d. F. and Shine, K. P.: Radiative forcing and temperature trends from stratospheric ozone changes, J. Geophys. Res.-Atmos.,
590   102, 10 841–10 855, https://doi.org/10.1029/96JD03510, https://agupubs.onlinelibrary.wiley.com/doi/abs/10.1029/96JD03510, 1997.

Ghan, S.: Technical Note: Estimating aerosol effects on cloud radiative forcing, Atmos. Chem. Phys., 13, 9971–9974,
https://doi.org/10.5194/acp-13-9971-2013, http://www.atmos-chem-phys.net/13/9971/2013/, 2013.

Gidden, M. J., Riahi, K., Smith, S. J., Fujimori, S., Luderer, G., Kriegler, E., van Vuuren, D. P., van den Berg, M., Feng, L., Klein, D., Calvin,
K., Doelman, J. C., Frank, S., Fricko, O., Harmsen, M., Hasegawa, T., Havlik, P., Hilaire, J., Hoesly, R., Horing, J., Popp, A., Stehfest,
595   E., and Takahashi, K.: Global emissions pathways under different socioeconomic scenarios for use in CMIP6: a dataset of harmonized
emissions trajectories through the end of the century, Geosci. Model Dev., 12, 1443–1475, https://doi.org/10.5194/gmd-12-1443-2019,
https://www.geosci-model-dev.net/12/1443/2019/, 2019.

Gregory, J., Ingram, W., Palmer, M., Jones, G., Stott, P., Thorpe, R., Lowe, J., Johns, T., and Williams, K.: A new method for diagnosing
radiative forcing and climate sensitivity, Geophys. Res. Lett., 31, https://doi.org/10.1029/2003GL018747, 2004.

600 Gregory, J. M., Andrews, T., and Good, P.: The inconstancy of the transient climate response parameter under increasing CO2, Philos. T. R.
Soc. A, 373, https://doi.org/10.1098/rsta.2014.0417, 2015.

Gryspeerdt, E., Mülmenstädt, J., Gettelman, A., Malavelle, F. F., Morrison, H., Neubauer, D., Partridge, D. G., Stier, P., Takemura, T.,
Wang, H., Wang, M., and Zhang, K.: Surprising similarities in model and observational aerosol radiative forcing estimates, Atmo-
spheric Chemistry and Physics Discussions, 2019, 1–18, https://doi.org/10.5194/acp-2019-533, https://www.atmos-chem-phys-discuss.
605   net/acp-2019-533/, 2019.

Hansen, J., Sato, M., Ruedy, R., Nazarenko, L., Lacis, A., Schmidt, G. A., Russell, G., Aleinov, I., Bauer, M., Bauer, S., Bell, N., Cairns,
B., Canuto, V., Chandler, M., Cheng, Y., Del Genio, A., Faluvegi, G., Fleming, E., Friend, A., Hall, T., Jackman, C., Kelley, M., Kiang,
N., Koch, D., Lean, J., Lerner, J., Lo, K., Menon, S., Miller, R., Minnis, P., Novakov, T., Oinas, V., Perlwitz, J., Perlwitz, J., Rind, D.,
Romanou, A., Shindell, D., Stone, P., Sun, S., Tausnev, N., Thresher, D., Wielicki, B., Wong, T., Yao, M., and Zhang, S.: Efficacy of
610   climate forcings, J. Geophys. Res.-Atmos., 110, https://doi.org/10.1029/2005JD005776, d18104, 2005.

Haustein, K., Allen, M., Forster, P., Otto, F., Mitchell, D., Matthews, H., and Frame, D.: A real-time Global Warming Index, Scientific
Reports, 7, 15 417, 2017.

Held, I. M. and Soden, B. J.: Water vapor feedback and global warming, Annu. Rev. Energ. Env., 25, 441–475,
https://doi.org/10.1146/annurev.energy.25.1.441, 2000.

615 Held, I. M., Guo, H., Adcroft, A., Dunne, J. P., Horowitz, L. W., Krasting, J., Shevliakova, E., Winton, M., Zhao, M., Bushuk, M., Witten-
berg, A. T., Wyman, B., Xiang, B., Zhang, R., Anderson, W., Balaji, V., Donner, L., Dunne, K., Durachta, J., Gauthier, P. P. G., Ginoux,
P., Golaz, J.-C., Griffies, S. M., Hallberg, R., Harris, L., Harrison, M., Hurlin, W., John, J., Lin, P., Lin, S.-J., Malyshev, S., Menzel,
R., Milly, P. C. D., Ming, Y., Naik, V., Paynter, D., Paulot, F., Rammaswamy, V., Reichl, B., Robinson, T., Rosati, A., Seman, C., Sil-
vers, L. G., Underwood, S., and Zadeh, N.: Structure and Performance of GFDL's CM4.0 Climate Model, J. Adv. Model. Earth Sy.,
620   https://doi.org/10.1029/2019MS001829, 2019.

Hoesly, R. M., Smith, S. J., Feng, L., Klimont, Z., Janssens-Maenhout, G., Pitkanen, T., Seibert, J. J., Vu, L., Andres, R. J., Bolt, R. M.,
Bond, T. C., Dawidowski, L., Kholod, N., Kurokawa, J.-I., Li, M., Liu, L., Lu, Z., Moura, M. C. P., O'Rourke, P. R., and Zhang, Q.:
Historical (1750–2014) anthropogenic emissions of reactive gases and aerosols from the Community Emissions Data System (CEDS),
Geosci. Model Dev., 11, 369–408, https://doi.org/10.5194/gmd-11-369-2018, 2018.

625 Johnson, B. T., Haywood, J. M., and Hawcroft, M. K.: Are Changes in Atmospheric Circulation Important for Black Carbon Aerosol Impacts on Clouds, Precipitation, and Radiation?, J. Geophys. Res.-Atmos., 124, 7930–7950, https://doi.org/10.1029/2019JD030568, https://agupubs.onlinelibrary.wiley.com/doi/abs/10.1029/2019JD030568, 2019.

Jonko, A. K., Shell, K. M., Sanderson, B. M., and Danabasoglu, G.: Climate Feedbacks in CCSM3 under Changing CO2 Forcing. Part II: Variation of Climate Feedbacks and Sensitivity with Forcing, J. Climate, 26, 2784–2795, https://doi.org/10.1175/JCLI-D-12-00479.1,
630 2013.

Kamae, Y. and Watanabe, M.: On the robustness of tropospheric adjustment in CMIP5 models, Geophysical Research Letters, 39, https://doi.org/10.1029/2012GL054275, 2012.

Kirkevåg, A., Grini, A., Olivié, D., Seland, Ø., Alterskjær, K., Hummel, M., Karset, I. H. H., Lewinschal, A., Liu, X., Makkonen, R., Bethke, I., Griesfeller, J., Schulz, M., and Iversen, T.: A production-tagged aerosol module for Earth system models, OsloAero5.3 –
635 extensions and updates for CAM5.3-Oslo, Geosci. Model Dev., 11, 3945–3982, https://doi.org/10.5194/gmd-11-3945-2018, https://www.geosci-model-dev.net/11/3945/2018/, 2018.

Klein, S. and Jakob, C.: Validation and Sensitivities of Frontal Clouds Simulated by the ECMWF Model, Mon. Weather Rev., 127, 2514–2531, https://doi.org/10.1175/1520-0493(1999)127<2514:VASOFC>2.0.CO;2, 1999.

Lamarque, J.-F., Bond, T. C., Eyring, V., Granier, C., Heil, A., Klimont, Z., Lee, D., Liousse, C., Mieville, A., Owen, B., Schultz, M. G.,
640 Shindell, D., Smith, S. J., Stehfest, E., Van Aardenne, J., Cooper, O. R., Kainuma, M., Mahowald, N., McConnell, J. R., Naik, V., Riahi, K., and van Vuuren, D. P.: Historical (1850–2000) gridded anthropogenic and biomass burning emissions of reactive gases and aerosols: methodology and application, Atmos. Chem. and Phys., 10, 7017–7039, https://doi.org/10.5194/acp-10-7017-2010, https://www.atmos-chem-phys.net/10/7017/2010/, 2010.

Loeb, N. G., Doelling, D. R., Wang, H., Su, W., Nguyen, C., Corbett, J. G., Liang, L., Mitrescu, C., Rose, F. G., and Kato, S.: Clouds and
645 the Earth's Radiant Energy System (CERES) Energy Balanced and Filled (EBAF) Top-of-Atmosphere (TOA) Edition-4.0 Data Product, J. Climate, 31, 895–918, https://doi.org/10.1175/JCLI-D-17-0208.1, 2018.

Mauritsen, T., Bader, J., Becker, T., Behrens, J., Bittner, M., Brokopf, R., Brovkin, V., Claussen, M., Crueger, T., Esch, M., Fast, I., Fiedler, S., Fläschner, D., Gayler, V., Giorgetta, M., Goll, D. S., Haak, H., Hagemann, S., Hedemann, C., Hohenegger, C., Ilyina, T., Jahns, T., Jimenéz-de-la Cuesta, D., Jungclaus, J., Kleinen, T., Kloster, S., Kracher, D., Kinne, S., Kleberg, D., Lasslop, G., Kornblueh, L.,
650 Marotzke, J., Matei, D., Meraner, K., Mikolajewicz, U., Modali, K., Möbis, B., Müller, W. A., Nabel, J. E. M. S., Nam, C. C. W., Notz, D., Nyawira, S.-S., Paulsen, H., Peters, K., Pincus, R., Pohlmann, H., Pongratz, J., Popp, M., Raddatz, T. J., Rast, S., Redler, R., Reick, C. H., Rohrschneider, T., Schemann, V., Schmidt, H., Schnur, R., Schulzweida, U., Six, K. D., Stein, L., Stemmler, I., Stevens, B., von Storch, J.-S., Tian, F., Voigt, A., Vrese, P., Wieners, K.-H., Wilkenskjeld, S., Winkler, A., and Roeckner, E.: Developments in the MPI-M Earth System Model version 1.2 (MPI-ESM1.2) and Its Response to Increasing CO2, J. Adv. Model. Earth Sy., 11, 998–1038,
655 https://doi.org/10.1029/2018MS001400, 2019.

Meinshausen, M., Vogel, E., Nauels, A., Lorbacher, K., Meinshausen, N., Etheridge, D. M., Fraser, P. J., Montzka, S. A., Rayner, P. J., Trudinger, C. M., Krummel, P. B., Beyerle, U., Canadell, J. G., Daniel, J. S., Enting, I. G., Law, R. M., Lunder, C. R., O'Doherty, S., Prinn, R. G., Reimann, S., Rubino, M., Velders, G. J. M., Vollmer, M. K., Wang, R. H. J., and Weiss, R.: Historical greenhouse gas concentrations for climate modelling (CMIP6), Geosci. Model Dev., 10, 2057–2116, https://doi.org/10.5194/gmd-10-2057-2017, https:
660 //www.geosci-model-dev.net/10/2057/2017/, 2017.

Mülmenstädt, J., Gryspeerdt, E., Salzmann, M., Ma, P.-L., Dipu, S., and Quaas, J.: Separating radiative forcing by aerosol–cloud interactions and fast cloud adjustments in the ECHAM-HAMMOZ aerosol–climate model using the method of partial radiative perturbations, Atmo-

spheric Chemistry and Physics Discussions, 2019, 1–20, https://doi.org/10.5194/acp-2018-1304, https://www.atmos-chem-phys-discuss.net/acp-2018-1304/, 2019.

665   Myhre, G., Shindell, D., Bréon, F.-M., Collins, W., Fuglestvedt, J., Huang, J., Koch, D., Lamarque, J.-F., Lee, D., Mendoza, B., Nakajima, T., Robock, A., Stephens, G., Takemura, T., and Zhang, H.: Anthropogenic and Natural Radiative Forcing, in: Climate Change 2013: The Physical Science Basis. Contribution of Working Group I to the Fifth Assessment Report of the Intergovernmental Panel on Climate Change, edited by Stocker, T., Qin, D., Plattner, G.-K., Tignor, M., Allen, S., Boschung, J., Nauels, A., Xia, Y., Bex, V., and Midgley, P., pp. 659–740, Cambridge University Press, Cambridge, United Kingdom and New York, NY, USA, 2013.

670   Myhre, G., Forster, P., Samset, B., Hodnebrog, Ø., Sillmann, J., Aalbergsjø, S., Andrews, T., Boucher, O., Faluvegi, G., Fläschner, D., , Iversen, T., Kasoar, M., Kharin, V., Kirkevå g, A., Lamarque, J.-F., Olivié, D., Richardson, T. B., Shindell, D., Shine, K. P., Stjern, C. W., Takemura, T., Voulgarakis, A., and Zwiers, F.: PDRMIP: A precipitation driver and response model intercomparison project—Protocol and preliminary results, B. Am. Meteorol. Soc., 98, 1185–1198, 2017.

O'Connor, F., Abraham, N. L., Dalvi, M., Folberth, G., Griffiths, P., Hardacre, C., Keeble, J., Jamil, O., Johnson, B., Kahana, R., Kim, B.,
675   Manners, J., Morgenstern, O., Mulcahy, J. P., Robertson, E., Seo, J., Shim, S., Teixeira, J. C., Turnock, S., Williams, J., Wiltshire, A., and Zeng, G.: Pre-industrial to present-day anthropogenic effective radiative forcings (ERFs) from UKESM1, J. Adv. Model. Earth Sy., submitted.

Pincus, R., Mlawer, E. J., Oreopoulos, L., Ackerman, A. S., Baek, S., Brath, M., Buehler, S. A., Cady-Pereira, K. E., Cole, J. N. S., Dufresne, J.-L., Kelley, M., Li, J., Manners, J., Paynter, D. J., Roehrig, R., Sekiguchi, M., and Schwarzkopf, D. M.: Radiative flux and forcing
680   parameterization error in aerosol-free clear skies, Geophys. Res. Lett., 42, 5485–5492, https://doi.org/10.1002/2015GL064291, 2015.

Pincus, R., Forster, P. M., and Stevens, B.: The Radiative Forcing Model Intercomparison Project (RFMIP): experimental protocol for CMIP6, Geosci. Model Dev., 9, 3447–3460, https://doi.org/10.5194/gmd-9-3447-2016, 2016.

Richardson, T., Forster, P., Maycock, A., Smith, C., Wood, T., Andrews, T., Boucher, O., Faluvegi, G., Fläschner, D., Hodnebrog, O., Kasoar, M., Kirkevag, A., Lamarque, J.-F., Mülmenstädt, J., Olivié, D., Samset, B., Shawki, D., Shindell, D., Takemura, T., and Voulgarakis, A.:
685   Efficacy of climate forcings in PDRMIP models, J. Geophys. Res., 124, https://doi.org/https://doi.org/10.1029/2019JD030581, 2019.

Rossow, W. B., Walker, A. W., Beuschel, D. E., and Roiter, M. D.: International Satellite Cloud Climatology Project (ISCCP) Documentation of New Cloud Datasets, 1996.

Santer, B. D., Wehner, M. F., Wigley, T. M. L., Sausen, R., Meehl, G. A., Taylor, K. E., Ammann, C., Arblaster, J., Washington, W. M., Boyle, J. S., and Brüggemann, W.: Contributions of Anthropogenic and Natural Forcing to Recent Tropopause Height Changes, Science,
690   301, 479–483, https://doi.org/10.1126/science.1084123, 2003.

Schmidt, G. A., Kelley, M., Nazarenko, L., Ruedy, R., Russell, G. L., Aleinov, I., Bauer, M., Bauer, S. E., Bhat, M. K., Bleck, R., Canuto, V., Chen, Y.-H., Cheng, Y., Clune, T. L., Del Genio, A., de Fainchtein, R., Faluvegi, G., Hansen, J. E., Healy, R. J., Kiang, N. Y., Koch, D., Lacis, A. A., LeGrande, A. N., Lerner, J., Lo, K. K., Matthews, E. E., Menon, S., Miller, R. L., Oinas, V., Oloso, A. O., Perlwitz, J. P., Puma, M. J., Putman, W. M., Rind, D., Romanou, A., Sato, M., Shindell, D. T., Sun, S., Syed, R. A., Tausnev, N., Tsigaridis, K., Unger,
695   N., Voulgarakis, A., Yao, M.-S., and Zhang, J.: Configuration and assessment of the GISS ModelE2 contributions to the CMIP5 archive, J. Adv. Model. Earth Syst., 6, 141–184, https://doi.org/10.1002/2013MS000265, 2014.

Sellar, A. A., Jones, C. G., Mulcahy, J., Tang, Y., Yool, A., Wiltshire, A., O'Connor, F. M., Stringer, M., Hill, R., Palmieri, J., Woodward, S., de Mora, L., Kuhlbrodt, T., Rumbold, S., Kelley, D. I., Ellis, R., Johnson, C. E., Walton, J., Abraham, N. L., Andrews, M. B., Andrews, T., Archibald, A. T., Berthou, S., Burke, E., Blockley, E., Carslaw, K., Dalvi, M., Edwards, J., Folberth, G. A., Gedney, N., Griffiths,
700   P. T., Harper, A. B., Hendry, M. A., Hewitt, A. J., Johnson, B., Jones, A., Jones, C. D., Keeble, J., Liddicoat, S., Morgenstern, O., Parker,

R. J., Predoi, V., Robertson, E., Siahaan, A., Smith, R. S., Swaminathan, R., Woodhouse, M. T., Zeng, G., and Zerroukat, M.: UKESM1: Description and evaluation of the UK Earth System Model, J. Adv. Model. Earth Sy., https://doi.org/10.1029/2019MS001739, 2019.

Sherwood, S. C., Bony, S., Boucher, O., Bretherton, C., Forster, P. M., Gregory, J. M., and Stevens, B.: Adjustments in the Forcing-Feedback Framework for Understanding Climate Change, B. Am. Meteorol. Soc., 96, 217–228, https://doi.org/10.1175/BAMS-D-13-00167.1, 2015.

705 Shine, K. P., Cook, J., Highwood, E. J., and Joshi, M. M.: An alternative to radiative forcing for estimating the relative importance of climate change mechanisms, Geophys. Res. Lett., 30, https://doi.org/10.1029/2003GL018141, 2047, 2003.

Smith, C. J., Kramer, R. J., Myhre, G., Forster, P. M., Soden, B. J., Andrews, T., Boucher, O., Faluvegi, G., Fläschner, D., Hodnebrog, O., Kasoar, M., Kharin, V., Kirkevåg, A., Lamarque, J.-F., Mülmenstädt, J., Olivié, D., Richardson, T., Samset, B. H., Shindell, D., Stier, P., Takemura, T., Voulgarakis, A., and Watson-Parris, D.: Understanding Rapid Adjustments to Diverse Forcing Agents, Geophys. Res. Lett.,
710 45, 12,023–12,031, https://doi.org/10.1029/2018GL079826, 2018.

Smith, C. J., Kramer, R. J., and Sima, A.: The HadGEM3-GA7.1 radiative kernel: the importance of a well-resolved stratosphere, Earth Syst. Sci. Data, submitted.

Soden, B., Held, I., Colman, R., Shell, K., Kiehl, J., and Shields, C.: Quantifying Climate Feedbacks Using Radiative Kernels, J. Climate, 21, 3504–3520, https://doi.org/10.1175/2007JCLI2110.1, 2008.

715 Soden, B. J., Collins, W. D., and Feldman, D. R.: Reducing uncertainties in climate models, Science, 361, 326–327, https://doi.org/10.1126/science.aau1864, 2018.

Stevens, B., Fiedler, S., Kinne, S., Peters, K., Rast, S., Müsse, J., Smith, S. J., and Mauritsen, T.: MACv2-SP: a parameterization of anthropogenic aerosol optical properties and an associated Twomey effect for use in CMIP6, Geosci. Model Dev., 10, 433–452, https://doi.org/10.5194/gmd-10-433-2017, https://www.geosci-model-dev.net/10/433/2017/, 2017.

720 Stjern, C. W., Samset, B. H., Myhre, G., Forster, P. M., Hodnebrog, Ø., Andrews, T., Boucher, O., Faluvegi, G., Iversen, T., Kasoar, M., Kharin, V., Kirkevåg, A., Lamarque, J.-F., Olivié, D., Richardson, T., Shawki, D., Shindell, D., Smith, C. J., Takemura, T., and Voulgarakis, A.: Rapid Adjustments Cause Weak Surface Temperature Response to Increased Black Carbon Concentrations, J. Geophys. Res.-Atmos., 122, 11,462–11,481, https://doi.org/10.1002/2017JD027326, 2017.

Swart, N. C., Cole, J. N. S., Kharin, V. V., Lazare, M., Scinocca, J. F., Gillett, N. P., Anstey, J., Arora, V., Christian, J. R., Hanna, S., Jiao, Y.,
725 Lee, W. G., Majaess, F., Saenko, O. A., Seiler, C., Seinen, C., Shao, A., Sigmond, M., Solheim, L., von Salzen, K., Yang, D., and Winter, B.: The Canadian Earth System Model version 5 (CanESM5.0.3), Geosci. Model Dev., 12, 4823–4873, https://doi.org/10.5194/gmd-12-4823-2019, https://www.geosci-model-dev.net/12/4823/2019/, 2019.

Séférian, R., Nabat, P., Michou, M., Saint-Martin, D., Voldoire, A., Colin, J., Decharme, B., Delire, C., Berthet, S., Chevallier, M., Sénési, S., Franchisteguy, L., Vial, J., Mallet, M., Joetzjer, E., Geoffroy, O., Guérémy, J.-F., Moine, M.-P., Msadek, R., Ribes, A., Rocher, M.,
730 Roehrig, R., Salas-y Mélia, D., Sanchez, E., Terray, L., Valcke, S., Waldman, R., Aumont, O., Bopp, L., Deshayes, J., Éthé, C., and Madec, G.: Evaluation of CNRM Earth-System model, CNRM-ESM 2-1: role of Earth system processes in present-day and future climate, J. Adv. Model. Earth Sy., https://doi.org/10.1029/2019MS001791, 2019.

Tang, T., Shindell, D., Faluvegi, G., Myhre, G., Olivié, D., Voulgarakis, A., Kasoar, M., Andrews, T., Boucher, O., Forster, P., Hodnebrog, O., Iversen, T., Kirkevåg, A., Lamarque, J.-F., Richardson, T., Samset, B., Stjern, C., Takemura, T., and Smith, C.: Comparison
735 of Effective Radiative Forcing Calculations Using Multiple Methods, Drivers, and Models, J. Geophys. Res.-Atmos., 124, 4382–4394, https://doi.org/10.1029/2018JD030188, https://agupubs.onlinelibrary.wiley.com/doi/abs/10.1029/2018JD030188, 2019.

Tatebe, H., Ogura, T., Nitta, T., Komuro, Y., Ogochi, K., Takemura, T., Sudo, K., Sekiguchi, M., Abe, M., Saito, F., Chikira, M., Watanabe, S., Mori, M., Hirota, N., Kawatani, Y., Mochizuki, T., Yoshimura, K., Takata, K., O'ishi, R., Yamazaki, D., Suzuki, T., Kurogi, M., Kataoka,

T., Watanabe, M., and Kimoto, M.: Description and basic evaluation of simulated mean state, internal variability, and climate sensitivity in MIROC6, Geosci. Model Dev., 12, 2727–2765, https://doi.org/10.5194/gmd-12-2727-2019, https://www.geosci-model-dev.net/12/2727/2019/, 2019.

Taylor, K., Crucifix, M., Braconnot, P., Hewitt, C., Doutriaux, C., Broccoli, A., Mitchell, J., and Webb, M.: Estimating shortwave radiative forcing and response in climate models, J. Climate, 20, 2530–2543, 2007.

Thornhill, G. D., Collins, W. J., Kramer, R. J., Olivié, D., O'Connor, F., Abraham, N. L., Deushi, M., Emmons, L., Forster, P., Horowitz, L., Keeble, J., Lamarque, J.-F., Michou, M., Mills, M., Mulcahy, J., Myhre, G., Nabat, P., Naik, V., Oshima, N., Schulz, M., Smith, C., Takemura, T., Tilmes, S., Wu, T., Zeng, G., and Zhang, J.: Effective Radiative forcing from emissions of reactive gases and aerosols—a multimodel comparison, Atmos. Chem. Phys., submitted.

Twomey, S.: The influence of pollution on the shortwave albedo of clouds, J. Atmos. Sci., 34, 1149–1152, 1977.

Vial, J., Dufresne, J.-L., and Bony, S.: On the interpretation of inter-model spread in CMIP5 climate sensitivity estimates, Clim. Dynam., 41, 3339–3362, https://doi.org/10.1007/s00382-013-1725-9, 2013.

Voldoire, A., Saint-Martin, D., Sénési, S., Decharme, B., Alias, A., Chevallier, M., Colin, J., Guérémy, J.-F., Michou, M., Moine, M.-P., Nabat, P., Roehrig, R., Salas y Mélia, D., Séférian, R., Valcke, S., Beau, I., Belamari, S., Berthet, S., Cassou, C., Cattiaux, J., Deshayes, J., Douville, H., Ethé, C., Franchistéguy, L., Geoffroy, O., Lévy, C., Madec, G., Meurdesoif, Y., Msadek, R., Ribes, A., Sanchez-Gomez, E., Terray, L., and Waldman, R.: Evaluation of CMIP6 DECK Experiments With CNRM-CM6-1, J. Adv. Model. Earth Sy., 11, 2177–2213, https://doi.org/10.1029/2019MS001683, 2019.

Webb, M., Senior, C., Bony, S., and Morcrette, J.-J.: Combining ERBE and ISCCP data to assess clouds in the Hadley Centre, ECMWF and LMD atmospheric climate models, Clim. Dynam., 17, 905–922, https://doi.org/10.1007/s003820100157, 2001.

Williams, K. D., Copsey, D., Blockley, E. W., Bodas-Salcedo, A., Calvert, D., Comer, R., Davis, P., Graham, T., Hewitt, H. T., Hill, R., Hyder, P., Ineson, S., Johns, T. C., Keen, A. B., Lee, R. W., Megann, A., Milton, S. F., Rae, J. G. L., Roberts, M. J., Scaife, A. A., Schiemann, R., Storkey, D., Thorpe, L., Watterson, I. G., Walters, D. N., West, A., Wood, R. A., Woollings, T., and Xavier, P. K.: The Met Office Global Coupled Model 3.0 and 3.1 (GC3.0 and GC3.1) Configurations, J. Adv. Model. Earth Sy., 10, 357–380, https://doi.org/10.1002/2017MS001115, 2018.

Yukimoto, S., Kawai, H., Koshiro, T., Oshima, N., Yoshida, K., Urakawa, S., Tsujino, H., Deushi, M., Tanaka, T., Hosaka, M., Yabu, S., Yoshimura, H., Shindo, E., Mizuta, R., Obata, A., Adachi, Y., and Ishii, M.: The Meteorological Research Institute Earth System Model Version 2.0, MRI-ESM2.0: Description and Basic Evaluation of the Physical Component, J. Meteorol. Soc. Jpn. Ser. II, 97, 931–965, https://doi.org/10.2151/jmsj.2019-051, 2019.

Zelinka, M., Klein, S., and Hartmann, D.: Computing and Partitioning Cloud Feedbacks Using Cloud Property Histograms. Part I: Cloud Radiative Kernels, J. Climate, 25, 3715–3735, https://doi.org/10.1175/JCLI-D-11-00248.1, 2012.

Zelinka, M. D., Andrews, T., Forster, P. M., and Taylor, K. E.: Quantifying components of aerosol-cloud-radiation interactions in climate models, J. Geophys. Res.-Atmos., 119, 7599–7615, https://doi.org/10.1002/2014JD021710, https://agupubs.onlinelibrary.wiley.com/doi/abs/10.1002/2014JD021710, 2014.

Zelinka, M. D., Myers, T. A., McCoy, D. T., Po-Chedley, S., Caldwell, P. M., Ceppi, P., Klein, S. A., and Taylor, K. E.: Causes of higher climate sensitivity in CMIP6 models, Geophysical Research Letters, accepted.